Investigation of corium melt interaction with NPP reactor vessel steel (METCOR)
Phase №2

PROGRESS REPORT

01/10/03 – 31/04/04

Investigation of the interaction between the suboxidized molten corium (c 32) with reactor vessel steel under neutral atmosphere above the melt ($T^{max}_{surf.steel}$ »1400°c). Test MC7.

Project title	**Investigation of Corium Melt Interaction with NPP Reactor Vessel Steel (METCOR, Phase 2)**, №833.2	
Contracting organization	ISTC	
File code	METCOR2/PRMB-02	
Project location	Aleksandrov Research Institute of Technologies of the RF Ministry for Atomic Energy Russia, 188540, Sosnovy Bor of Leningrad Oblast, NITI	
Project manager	Name	V.B. Khabensky
	Signature	
	Date	January, 2005

Authors

Professor	V.B. Khabensky
Doctor	S.V. Bechta
Doctor	V.S. Granovsky
	S.A. Vitol
	E.V. Krushinov
Professor, Associate member of the Russian Academy of Sciences	V.V. Gusarov
Professor	Yu.B. Petrov
Doctor	I.V. Kulagin
Doctor	D.B. Lopukh
Doctor	A.Yu. Pechenkov
Doctor	I.V. Pozniak
	V.G. Blizniuk
	V.R. Bulighin
	V.I. Almiashev
	E.K. Kalyago
	N.E. Kamensky
Doctor	S.Yu. Kotova
	I.A. Loghinov
	A.V. Lisenko
	A.P. Martinov
	V.V. Martinov
	E.V. Shevchenko

Abstract

The report presents the description and basic results of Test MC7 of the ISTC METCOR-2 Project carried out in the NITI, Sosnovy Bor, on the “Rasplav-3” test facility. The vessel steel ablation has been examined in the oxygen-free (argon) atmosphere during its long-term interaction with C-32 corium through the crust, the maximum temperature in the interaction zone being 1150 °C.

CONTENTS

Introduction

The results of test MC6 [8], in which corium-steel interaction was examined at a maximum temperature on the steel surface (approx. 1400 ^{o}C), enabled to determine that the final position of the interaction front boundary corresponds to 1120 ... 1200 ^{o}C. In order to check the influence of surface temperature on the kinetics and depth of steel corrosion test MC7 has been conducted, which is included into the METCOR-2 experimental matrix [2] and was discussed at the collaborators' meeting [1]. Similar to MC6, test MC7 was conducted in argon with corium of C-32 composition. A difference from MC6 was that in MC7 maximum temperature on the steel surface was kept at 1150 ºC.

1. Test description

1.1. Equipment

A modernized test facility [3] comprising a HF generator having the oscillatory power of 100 kW and current frequency 130 kHz was used. The melt was produced by the induction melting in a cold crucible [4]. The furnace schematics and its photograph are presented in Figs. 1.1, 1.2.

In order to evaluate heat fluxes from melt to specimen (11) and for cooling the zone, where the ultrasonic sensor (15) was attached to the specimen, two calorimeters were provided – a top calorimeter (12) and a bottom calorimeter (13). To exclude electromagnetic heating of the specimen the lower parts of crucible sections were welded together, and this arrangement served as an electromagnetic screen (18). Specimen was positioned in the crucible so that its top was 1 mm lower than the top of the welded sections. The gap between the specimen and crucible sections was filled with ZrO_2 powder (10) and pellets of molten ZrO_2 (9). An additional screening of specimen from electromagnetic heating was performed by using water-cooled movable screen (3). An argon-sparged water-cooled steel shaft (1) was used for the melt surface monitoring.

Figs. 1.3, 1.4 show the scheme and picture of the vessel steel 15Kh2HMFA-A specimen. Table 1.1 gives the locations of K-type thermocouple junctions in the specimen. In a 10 mm radius from the specimen axis the thermocouples were embedded into 1.5 mm-diameter channels, and in a 29 mm radius – into the 1.5 mm-wide carved grooves.

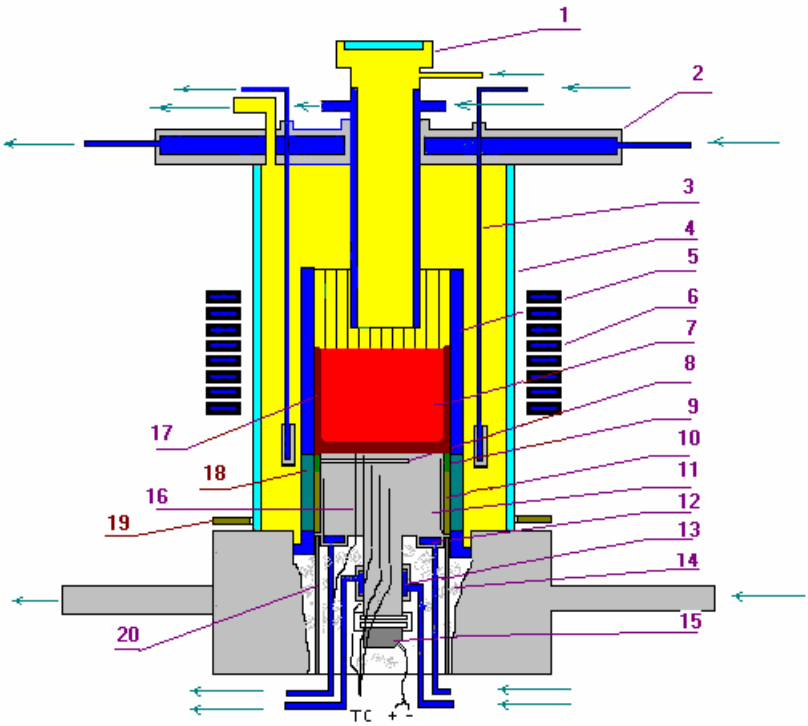

Fig. 1.1. IMCC furnace schematics

1 – water-cooled pyrometer shaft; 2 – water-cooled cover; 3 – water-cooled electromagnetic screen; 4 – quartz tube; 5 – crucible sections; 6 – inductor; 7 – melt; 8 – acoustic defect; 9 –molten ZrO_2 insulation; 10 –ZrO_2 powder; 11 – vessel steel specimen; 12 – top specimen calorimeter; 13 – bottom specimen calorimeter; 14 – kaolin wool insulation;; 15 –ultrasonic sensor; 16 – thermocouples; 17 – crust 18 – electromagnetic screen (crucible sections are welded); 19 – uncooled electromagnetic screen; 20 – cylindrical support of the specimen.

Fig. 1.2. IMCC furnace before the test

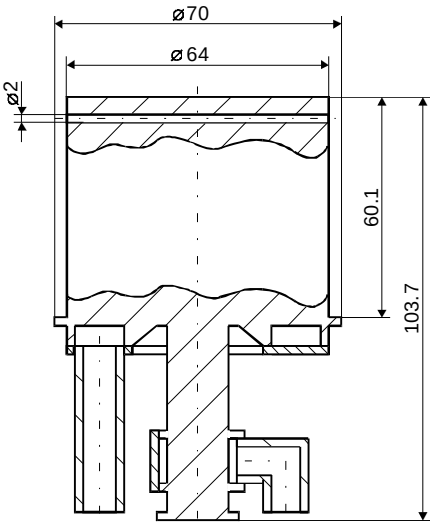

Fig. 1.3. Specimen sketch

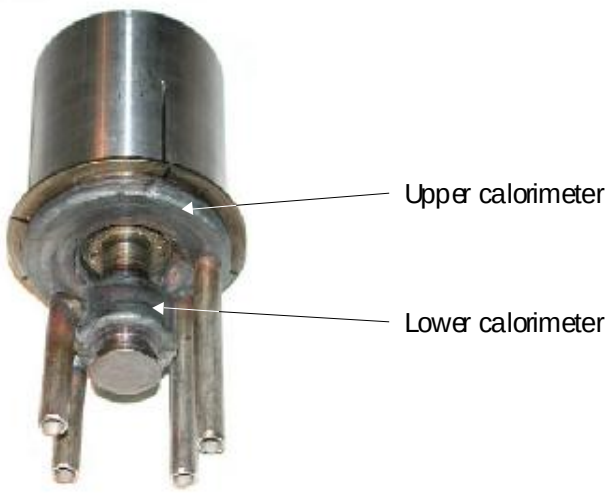

Fig. 1.4. Specimen photograph

Table 1.1.

Thermocouple hot junction locations in the vessel steel specimen

Thermocouple №	TC 01	TC 02	TC 03	TC 04	TC 05	TC 06	TC 07	TC 08	TC 09	TC 10	TC 11	TC 12	TC 13
Angle, α, degrees	0	270	180	225	90	315	45	135	270	180	45	315	45
Distance from the specimen axis to the junction, r, mm	10	10	10	10	10	10	10	29	29	29	29	29	7.5
Distance from the specimen top to the junction, h, mm	0.0	2.0	4.0	6.0	6.0	8.0	20.0	0.0	2.0	4.0	20.0	40.0	103.7

The chosen temperature level on the corium-steel interaction interface, 1150^{o}C, enabled to change the frequency of ultrasonic sensor to 5 MHz and to increase the accuracy of corrosion depth and rate measurements.

The furnace was insulated with quartz tube (4) and water-cooled cover (2).

Gas-aerosol sampling system (Fig. 1.5) was used to monitor the oxygen partial pressure in the furnace off-gases and to make the test mass balance. Oxygen content in the off-gas was measured with electrochemical sensor (12).

Alternatively switched large-area filters (9) were used to remove aerosols from the off-gas. Gas flow parameters (flow rate, pressure) were measured by electromechanical flow-rate meters G1, G2 of OR-40/C-type, rotameter G3, “Korund-DIV” P1-P4 pressure sensor. Silica gel dehumidifier (2) was incorporated into the furnace inlet scheme to dry the incoming gas

completely. Argon was fed into the furnace through shaft (4), which also improved the quality of pyrometric measurements and video recording, because it blew aerosols off.

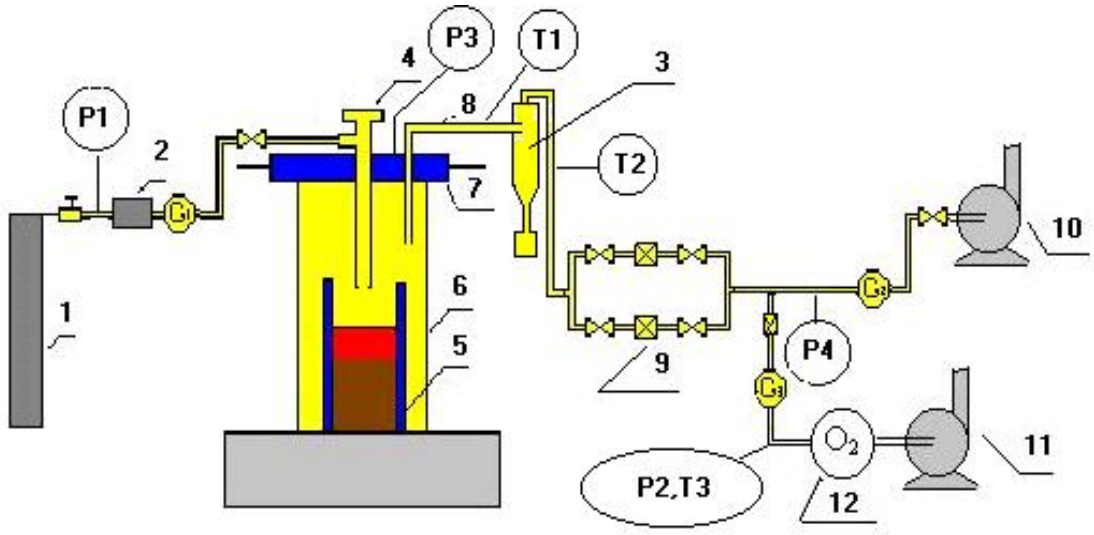

Fig.1.5. Gas in and out

1 – Ar tank; 2 – silica gel dehumidifier; 3 – cyclone; 4 - Pyrometer shaft; 5 - crucible; 6 – quartz tube; 7 – water-cooled cover; 8 – aerosol pathway; 9 - LAF filters; 10-fan; 11 - vacuum pump; 12 – oxygen sensor; P1-P4, pressure sensors; G1, G2– flow-rate meters, G3-rotameter; T1-T4 thermocouples

1.2. Materials

Charge was put into the crucible in argon atmosphere in accordance with a developed procedure. 150 g of corium was placed on the specimen top, the corium had C-27 composition (76.4%UO_2; 7.9% ZrO_2; 15.7%Zr), here and hereafter mass %), particle size ≤50 μm. Corium C-27 had been synthesized in argon in a separate test Pr1-MC6. This was followed by the addition of C-32 charge (76.00%UO_2; 9.33% ZrO_2; 14.67%Zr). Metallic zirconium was put inside the UO_2 - ZrO_2 $_{mixture}$ to ensure the required corium composition and for performing the startup heating.

The following materials were used in the test: vessel steel 15Kh2NMFA-A, uranium dioxide, zirconium oxide, metallic zirconium, argon. All materials were subjected to the analysis for the basic substance content. Additionally, the thermogravimetry method was applied to measure the oxygen/uranium ratio in the UO_2 powder, which was 2.0. Table 1.2 gives the composition of corium charge. Table 1.3 provides the data on composition and mass of the furnace charge components before melting.

The required fractions of UO_2 and corium were obtained by crushing tablets taken from fuel elements and C-32 ingot, which had been synthesized in Pr1-MC6, the crushing was performed in argon. The analysis of the average sample from the crushed ingot was performed by the XRF and specrophotometry.

In order to establish the oxygen-free atmosphere above the melt, argon belonging to the “extra pure” category was procured.

Table 1.2

Composition of corium charge components

Component	**Content of the basic substance, %**	**Admixtures, %**	**Note**
UO_2	> 99.0	Fe < 0.03; As < 0.0003; Cu < 0.01; phosphates < 0.002; chlorides < 0.003	Certificate data; thermogravimetry
ZrO_2	(ZrO_2+ HfO_2) > 99.3	Al_2O_3<0.03; Fe_2O_3<0.05; CaO<0.03; MgO<0.02; SiO_2<0.2; TiO_2<0.1; P_2O_5<0.15; (Na_2O+K_2O)<0.02	Certificate data
Zr	alloy H-1	Nb<1.0	XRF

Table 1.3

Composition and mass of charge components

Function	**Component**	**Fraction, mm**	**Mass, g**	**Mass%**
Crust	Corium C-27.0 (76.4%UO_2; 7.9% ZrO_2; 15.7%Zr)	< 50	158	8.5
Main charge	UO_2	< 500	1292.0	69.5
	ZrO_2	< 50	158.6	8.5
	Metallic zirconium, Zr	Pins 4 mm in diameter and 15 mm high	249.4	13.4
Total			**1858.0**	**100.0**

1.3. Experimental procedure

Furnace schematics, locations of TC hot junctions, initial materials and furnace charging procedure were similar to MC6. The only difference was in a changed particle size of ZrO_2 powder used as a charge (see 10 in Fig. 1, MC6 Report [8]). The furnace was sparged with argon during 10 minutes with a 10 l/min. flow-rate. It was followed by the startup heating and molten pool production, at this stage the specimen top was positioned lower than the inductor top by 20 mm, and vs. screen top – by 10 mm. After that the crucible and screen were not moved unlike in MC6. The specimen top temperature was stabilized by adjusting the generator power.

At the 3420th second the temperature on the specimen top reached approximately 1150ºC, and from that moment the vessel steel ablation kinetics was studied during 10 hours in the stabilized temperature regime. Fig. 1.7 presents the history of heat fluxes into the crucible, inductor and other furnace components. The readings of thermocouples in the steel specimen throughout the test are given in Fig. 1.8. Fig 1.9 presents the dynamics of power into the top and bottom calorimeters. The photographs of corium ingot in the cold crucible and corium ingot on the steel specimen after the crucible was disassembled are given in Figs. 1.10 and 1.11.

After the 10-hour exposure, at the 39450th second of the test, heating was disconnected and the ingot with specimen was cooled in argon.

Throughout the test the argon-sparged water-cooled shaft was used for the continuous melt temperature measurements, (Fig. 1.6) by the spectral-ratio pyrometer RAYTEK of the MR1SCSF series having the wave-lengths 0,75 - 1,1 μm – 0,95 - 1,1 μm. The melt surface was periodically recorded on video.

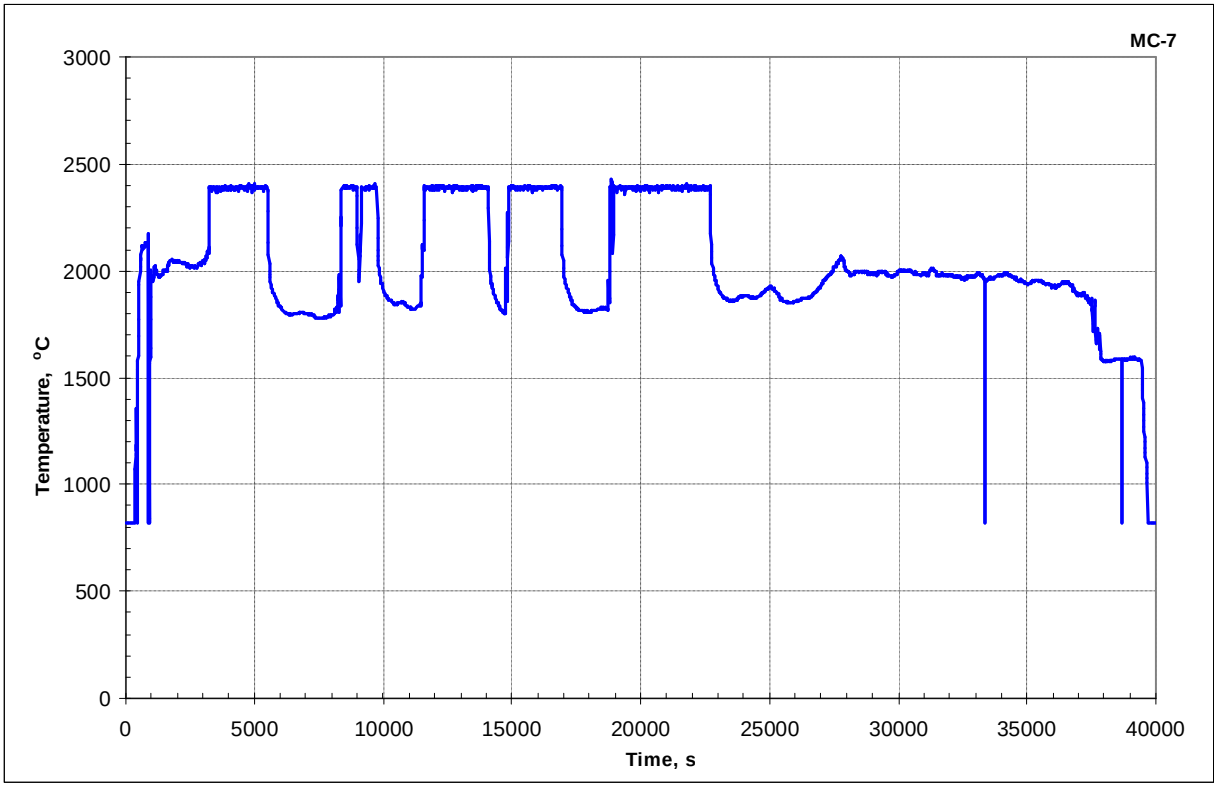

Fig. 1.6. Pyrometer readings

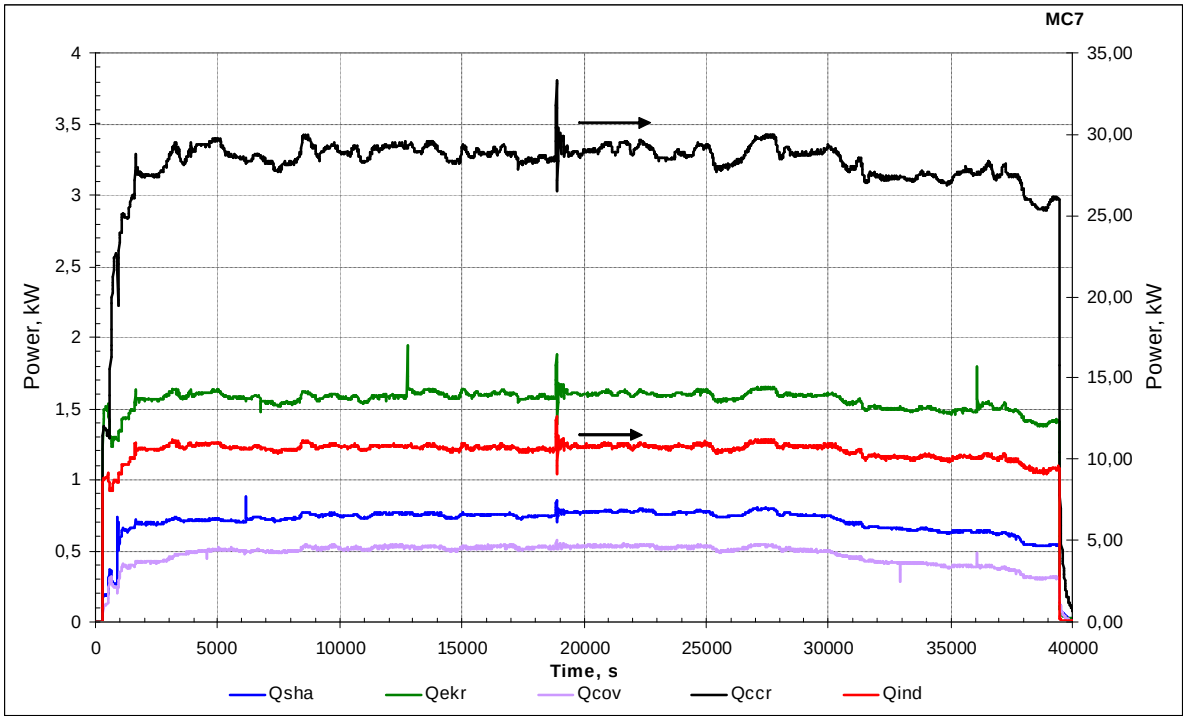

Fig. 1.7. Electric and heat power into furnace components

Q_{ccr} – electric and heat fluxes into the crucible; Q_{ind} – electric fluxes into the inductor; P_{shaft} – electric and heat fluxes into the shaft; Q_{ekr} – electric fluxes into the electromagnetic screen; Q_{cov} – electric and heat fluxes into the cover

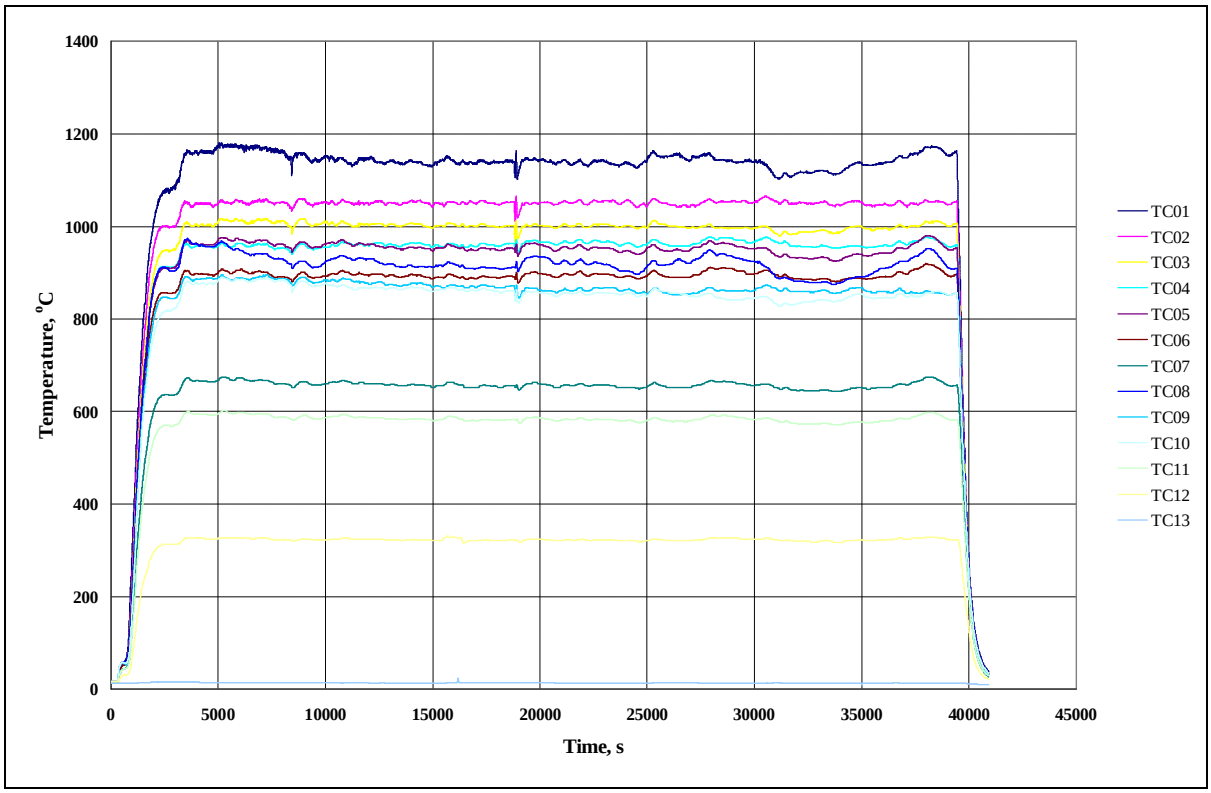

Fig. 1.8. Thermocouple readings during the test

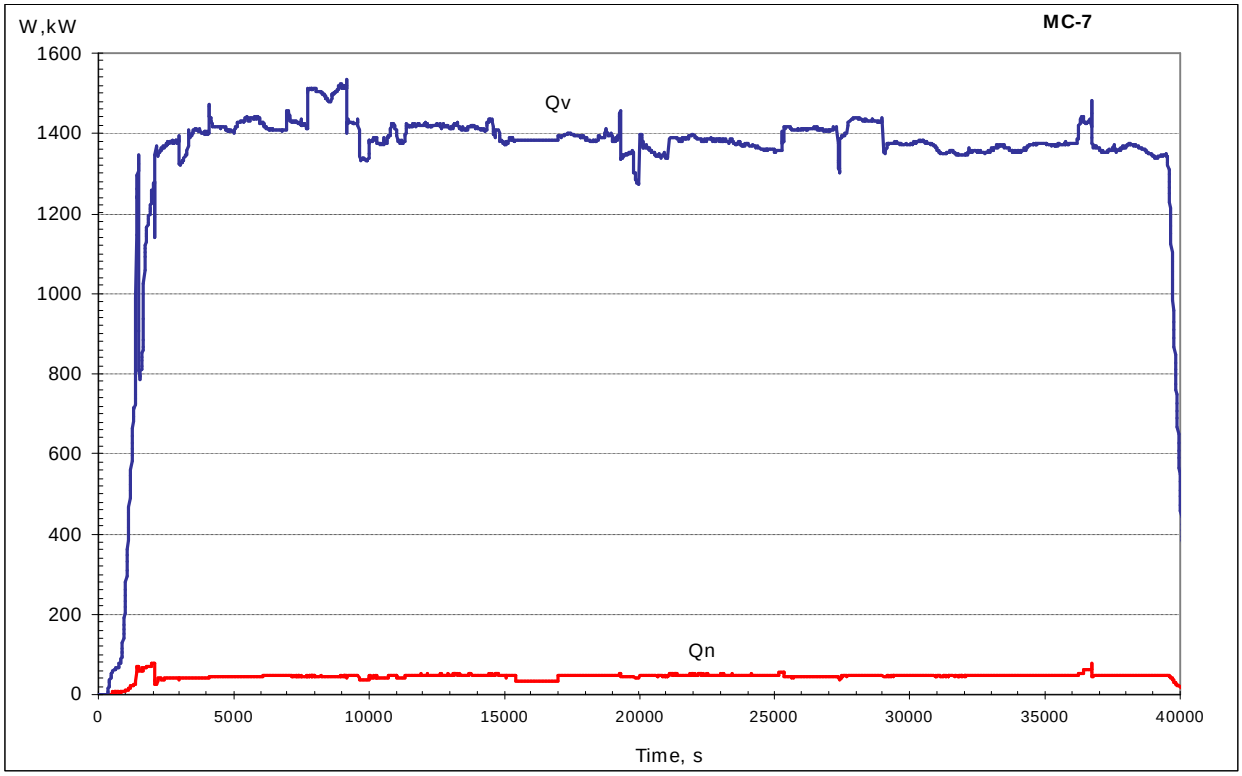

Fig. 1.9. Power into the top and bottom specimen calorimeters

Fig. 1.10. Corium ingot in the cold crucible

Fig. 1.11. Corium ingot on the steel specimen after the crucible disassembly

2. Posttest analysis

2.1. Physico-chemical analysis

2.1.1. Material balance of the test

In order to make the material balance the input charge components and melting products were analyzed for the content of basic components and weighed with accuracy up to 0.1 g.

Just like in MC6, corium produced in a separate pre-test Pr1-MC6 was used to simulate the crust on the steel specimen. Table 2.3.1 presents the results of the physico-chemical analysis of the average corium sample.

Table 2.1

Physico-chemical data of the average sample from the Pr1-MC6 ingot

Method	**XRF**			**Volumetry**	**Oxidation degree, C**
Element	**U**	**Zr**	**Admixtures and O***	Zr^0	
Average ingot sample, mass%	67.3	21.6	11.0	16.0	27.0

*-from the residue.

Material balance of components in MC7 is given in Table 2.2.

Table 2.2

MC7 material balance

Introduced into the melt, g		**Gathered after the test, g**	
Corium C-27.0 (76.4 Mass %UO_2, 7.9 mass % ZrO_2, 15.7 mass% Zr)	158.0	From the probe	3.3
UO_2	1292.0	Ingot and steel specimen*	3480±10
ZrO_2	158.6	Aerosols	9.8
Zr metallic	249.4	Spillages	54.1
Steel specimen	1692.6		
Σ	3550.6	**Σ**	**3550±10**

*) the specimen and corium ingot were incorporated into the resin matrix immediately after the test, for this reason the ingot mass was determined from the residue from the total charge mass.

2.1.2. X-ray fluorescence (XRF) of the witness specimen and melting products

The elemental composition of the witness-specimen and melting products was determined by the XRF method using the SPARK-1M/IBM PC spectrometer [9].

Similar to MC5 and MC6, the witness steel specimen, having the shape of a 40 mm diameter disc, was cut from a cylindrical block and subjected to the XRF analysis.

Table 2.3 presents the XRF data of the witness specimen and its comparison to the requirements of the Standard Specifications (TU, Russian acronym) of this vessel steel brand.

Table 2.3

XRF data on the 15Kh2NMFA-A witness specimen

TU, method of analysis	Concentration of chemical elements, % mass.											
	C	**Si**	**Mn**	**Cr**	**Ni**	**Mo**	**V**	**P**	**S**	**Cu**	**Co**	**As**
TU 108-765-78	0.13-0.18	0.17-0.37	0.30-0.60	1.8-2.3	1.0-1.5	0.5-0.7	0.10-0.12	<0.02	<0.02	<0.3	<0.03	<0.003
XRF	-	0.25	0.49	2.24	1.00	0.70	0.10	<0.02	-	0.07	<0.03	<0.003

The XRF data testify to the full compliance of steel used in the tests with TU 108-765-78 requirements.

2.1.3. Chemical analysis of molten products

After the test the corium ingot and steel specimen were incorporated into the epoxy resin matrix and cut along the axis. Fig. 2.5 shows the ingot axial section and locations where samples were taken.

The corium ingot half was cut again, after which the average samples of its top and bottom parts were produced; they were analyzed for the U^{+4}, U^{+6} content [10,11]. The average samples were produced by quartering and crushing down to the particle size of < 50 μm.

The following methodology is used for determining the microquantities of uranium (U^{+4}, U^{+6}) in corium samples. Its sensitivity is 0.04 μg/ml. The method is based the property of tetravalent U to form colored compounds with arsenazo III in 4 N HCl. The granulated zinc in presence of ascorbic acid is used for the reduction of uranium. At the interaction with arsenazo III, the tetravalent uranium forms a green complex; if the reagent is in excess, a multi-shade violet coloring is observed. The spectrophotometry gives best results at the 2-5-fold molar excess of the reagent. The coloring appears immediately and stays stable at least for 2 hours. The method enables to determine the content of tetravalent uranium and total content of uranium in the solution separately. The content of hexavalent uranium is calculated from the difference between uranium (IV) and total uranium content.

The volumetric method [12] was used for determining free zirconium in corium samples. The method is based on measuring the amount of hydrogen, which is liberated at the interaction of metallic zirconium present in corium with concentrated phosphoric acid. The reaction of interaction between metallic zirconium and concentrated phosphoric acid follows the scheme:

(dissolution of free zirconium in phosphoric acid accompanied by the generation of two moles of hydrogen per each gram-atom of zirconium)

$$Zr + 4H_3PO_4 = Zr(H_2PO_4)_4 + 2H_2\uparrow. \qquad (1)$$

Free zirconium was calculated from the volume of released hydrogen in the following way:

$$Zr_{св} = \frac{91{,}22 \cdot 273{,}15}{2 \cdot 22{,}416 \cdot 760} \cdot \left(\frac{V_2 \cdot P_2}{273{,}15 + t_2} - \frac{V_1 \cdot P_1}{273{,}15 + t_1} \right) \qquad (2),$$

where

91,22 – atomic weight of Zr

273,15 – absolute temperature of water freezing, K;

2241,60 – volume of one mole of hydrogen gas under temperature 273,15 K and 760 mm mercury column, l.

V_2 and V_1 – volumes of gas measured after and before the tested mixture dissolution, ml.

P_2 and P_1 - atmosphere pressure after and before the tested mixture dissolution, mm merc. col.

t_2 and t_1 – ambient air temperature measured after and before the tested mixture dissolution, ^oC.

The determination of free and total Zr enables to evaluate the zirconium oxidation degree (C_n) from:

$$C_n = (Zr_{total} - Zr_{free.}) / Zr_{total} * 100\%, \quad (3)$$

The content of metallic iron, Fe^0, was determined by the copper-sulfate method [13].

Table 2.4 presents the chemical analysis of the top and bottom parts of corium ingot.

Table 2.4

Chemical analysis of the corium ingot top and bottom

Method of detection	**Photocolorimetry (dissolution in H_2SO_4 and H_3PO_4)**			**Copper-sulfate method**	**Volumetric method**
Sample	**U^{4+}**	**U^{6+}**	**Fe^{2+}**	**Fe^0**	**Zr^0**
	mass%				
Average corium sample (ingot bottom)	64.67	Not detected	0.55	0.078	14.15
Average corium sample (ingot top)	66.08	Not detected	0.42	0.069	13.45

Table 2.5 gives the errors of different analyses

Table 2.5

Analyses errors

Element	**Error % rel.**	**Method of detection**
U^{+4}	5	Photocolorimetry
U^{+6}	5	Photocolorimetry
Zr^0 (met)	10	Volumetry
Fe^0	10	Copper - sulfate

2.1.4. Density of molten corium

The picnometric (bottle) density of molten corium was determined from the average sample, which was prepared by quartering and crushing down to particle size < 50 μm [14]. Distilled water was used as a picnometric liquid. The evaluation of molten corium density under normal conditions is presented in Table 2.6.

Table 2.6

Picnometric density of molten corium

Sample	Particle size of molten corium, mm	Bottle density, g/cm^3
Average corium sample (top part of ingot)	<50	8.81
Average corium sample (bottom part of ingot)		8.66

The density evaluation error was ± 0.02 g/cm^3.

The completed posttest physico-chemical analyses of MC7 corium ingot enable to make the following conclusions:

- the products of steel-corium C-32 interaction have partially migrated into the oxidic melt as a result of the mass-exchange processes on the metal-oxide boundary (Table 2.4.);

- the reduction of unbound zirconium in the melt in comparison to its initial inventory is the indicator of its partitioning between the molten pool and steel specimen.

2.2. Numeric modeling of the specimen temperature conditions

Similar to the MC5 and MC6 posttest analyses , in order to determine the temperature and heat flux density on the interaction boundary the specimen temperature field was calculated for the conditions close the stationary regime, from ~3420 to ~ 39000 s. In the calculations a finite-element numeric code was used, which applied the solution of a stationary heat conductivity equation in an axi-symmetrical formulation.

The following conditions were set as boundary:

1. Temperature on the internal surface of the top calorimeter, which in accordance with evaluations was ~ 100°C (insignificant evaluation error practically does not influence the calculation accuracy).
2. Temperature on the internal surface of the bottom calorimeter (20°C).
3. Temperature on the external surface of the outer insulation layer, which is assumed to be equal to the average temperature of the cooling water in the crucible.

METCOR-1 data [5] on heat conductivity of the 15Kh2NMFA-A steel of the specimen were used. In order to achieve the best agreement between the calculated and experimental temperature values in the TC junction locations in the specimen, the density of heat flux to the specimen top was varied in the calculations. At this, like in MC5 and MC6, the distribution of heat flux density along the radius was taken from the results of Pr1-MC6, and heat conductivity

of the insulating periphery layer was changed in comparison with the one used in MC5,6 calculations. It was done because of a different particle size of the insulating ZrO_2 powder.

Table 2.7 presents the averaged specimen thermocouple readings during the steady-state regime. The average power into the top calorimeter is 1393 W. Power into the bottom calorimeter is negligibly small.

Table 2.7

Averaged temperatures in the specimen

Thermocouple №	TCO1	TCO2	TCO3	TCO4	TCO5	TCO6
Average temperature, °C	1143	1051	1001	962	954	859
Root-mean-square value deviation, °C	15,3	4,4	7,2	6,2	11,1	7,0
Thermocouple №	TCO7	TCO8	TCO9	TCO10	TCO11	TCO12
Average temperature, °C	658	920	869	859	585	323
Root-mean-square value deviation, °C	6,8	20,0	11,4	13,8	6,6	2,6

The results of measurements are presented in Figs. 2.1 – 2.3. Fig. 2.1 shows the vertical distribution of experimental and calculated temperatures in the specimen on the 10 and 29 mm radii. Their comparison demonstrates a satisfactory agreement of the calculated and measured data. Fig. 2.2 gives the calculated radial distribution of temperatures on the specimen top. The maximum value in the center was 1153°C. Fig. 2.3 shows the temperature distribution in the axial section of the specimen. The same figure shows the boundary of the melt-specimen interaction zone, which was determined by the posttest analysis (see Section 2.3). The corresponding temperature boundary is 1030-1100 °C.

The calculated average densities of the heat flux to the specimen top and in the top center (155 mm in diameter, the ultra-sonic sensor sighting spot) are 0,82 MW/m^2 and 1,1 MW/m^2 respectively.

The calculated power into the top calorimeter is 1200 W, which has a ~ 15% difference from the measured value.

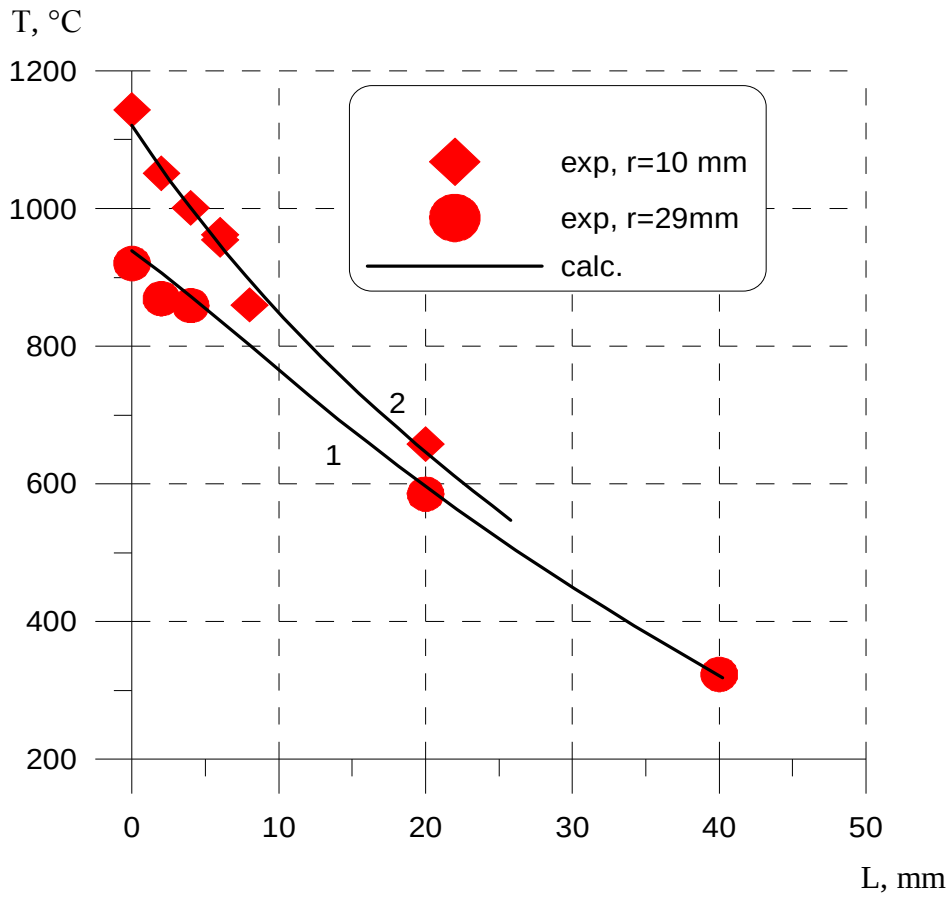

Fig. 2.1. Axial temperature distribution in the specimen

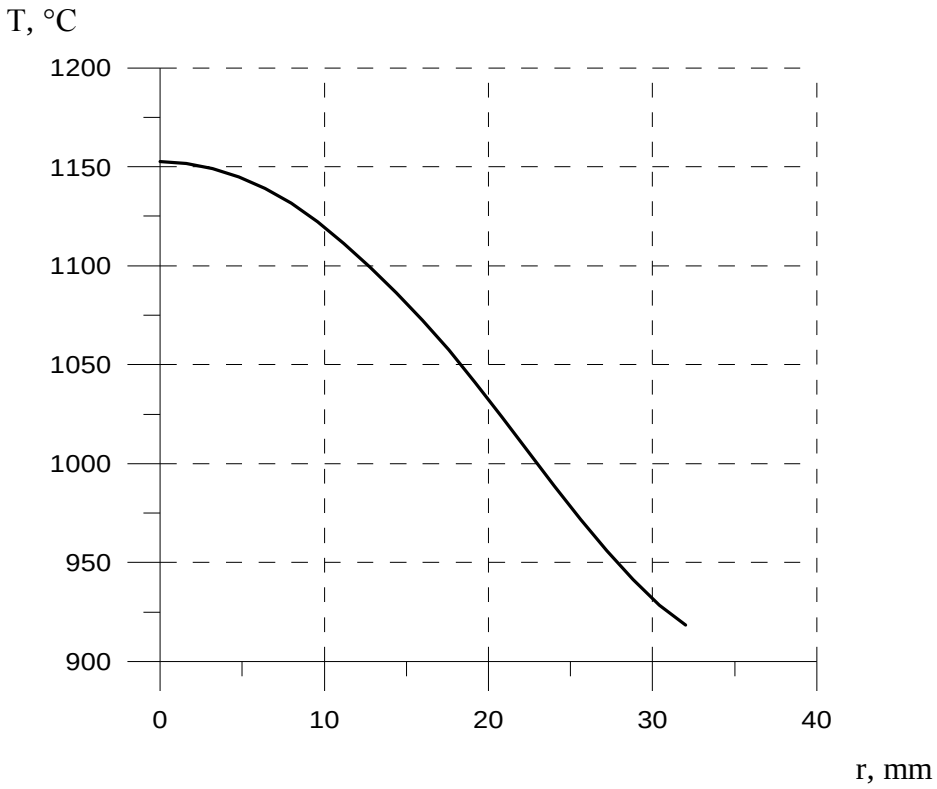

Fig. 2.2. Radial temperature distribution on the specimen top

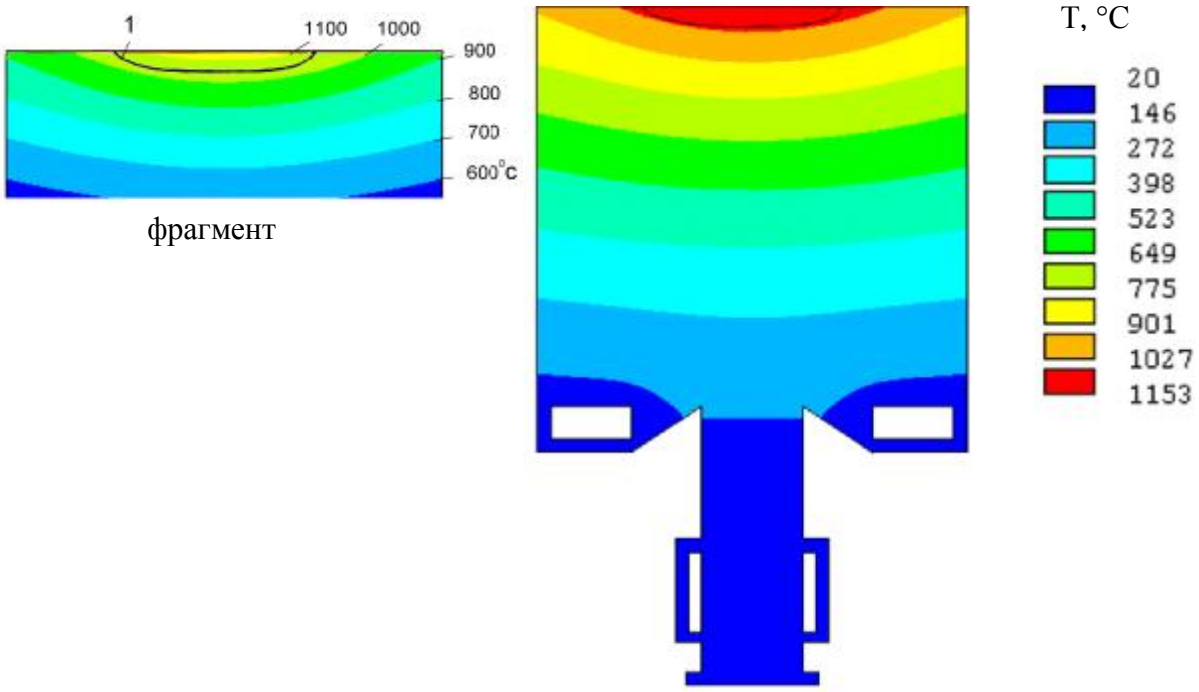

Fig. 2.3. Calculated temperature field in the specimen

1 – interaction zone boundary

2.3. Material studies

A 15Kh2NMFA-A steel specimen has been tested in MC7 (Fig. 1.4).

2.3.1. Metallography and direct specimen ablation measurements

Exact specimen dimensions were determined using the stereoscopic microscope MBS-9 (scale factor 14 μm, 50-fold magnification). Measurement locations are shown in Fig. 2.4.

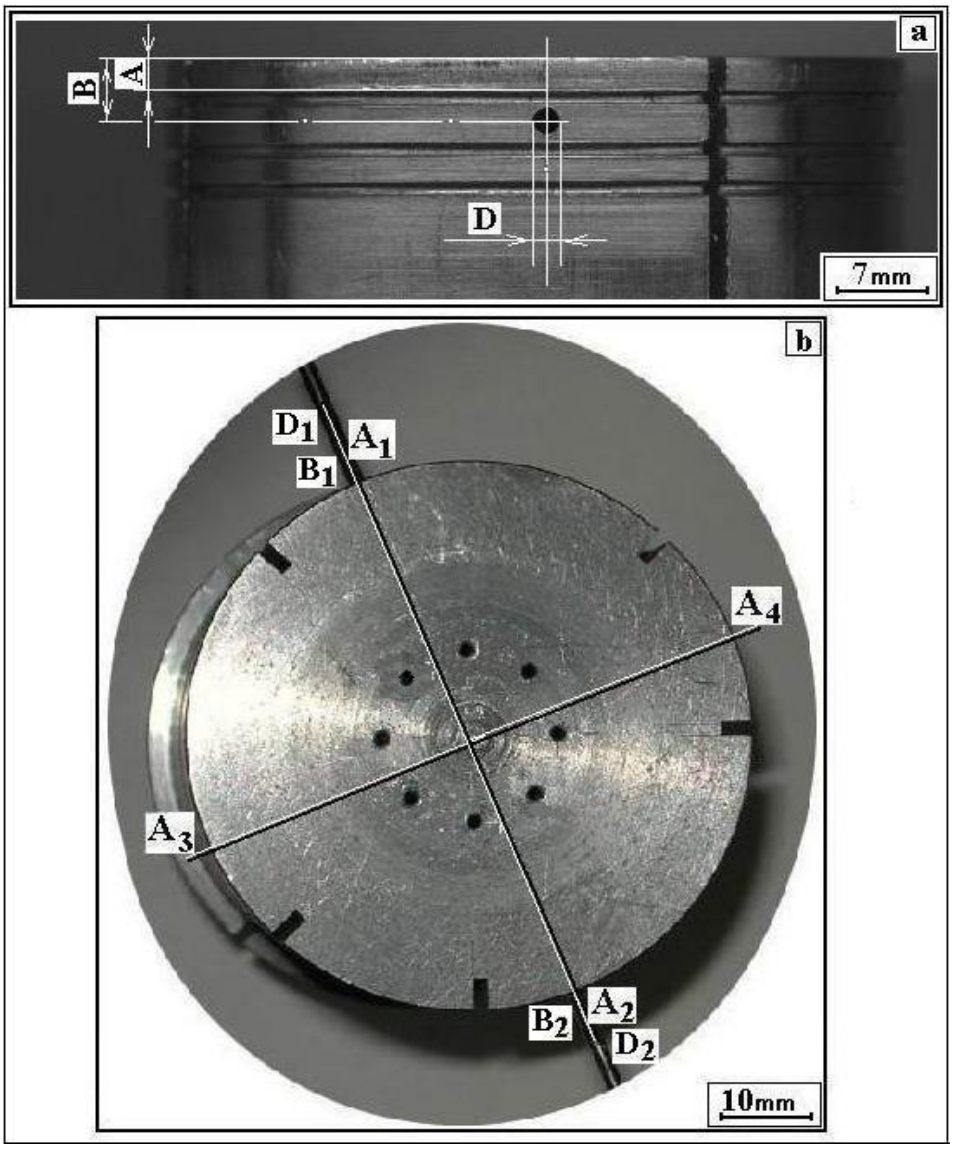

Fig. 2.4. Side surface (a) and top (b) of the MC7 steel specimen before the test

A (A_1, A_2, A_3, A_4), B (B_1, B_2), D (D_1, D_2)- measurement locations. A1 = 2.99 mm, A2 = 2.97 mm, A3 = 2.98 mm, A4 = 2.97 mm, B1 = 5.12 mm, B2 = 5.05 mm, D1 = 2.1 mm, D2 = 2.15 mm. Specimen length L = 103,7 mm

After the test the corium ingot and steel specimen were included into the epoxy resin matrix in order to prevent their separation and exclude the crumbling of fragile oxidic part

during cutting. The resulting block was cut across and along the axis for further studies. Fig. 2.5 shows the cut surface with locations of templates; Fig 2.5 c) shows the axial section of ingot A1-A2 (Fig. 2.4), and Fig. 2.5 b) – the section cut at a 4 mm distance from the axis.

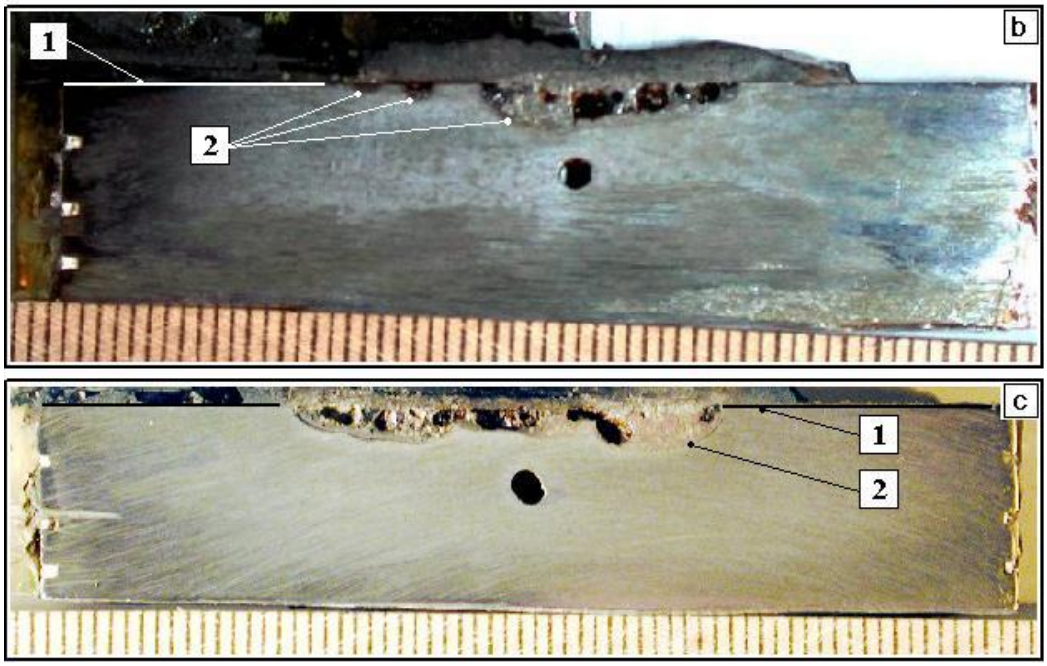

Fig. 2.5. Templates cut from the block in the interaction zone

The interaction zone depth was measured on the axial specimen section by the metallographic microscope METALLUX at the 100; 400 magnification and by the stereoscopic microscope MBS-9 at the 50^x and 100^x magnification. The scale factor of micrometer screw and object plate of microhardnessmeter is 0,01 mm (10 μm). The measurement error is ±10 μm; it was determined with stage micrometer. The position of the initial top plane was determined from the groove made in the specimen side surface at the distance of 2,98 mm from the top. After the measurements the specimen ablation profilograms were constructed (line 2 and line 3, Fig. 2.6). The maximum ablation depth was 3.1 mm. Along with that <3mm-wide pores were found in the interaction zone, Fig 2.7.

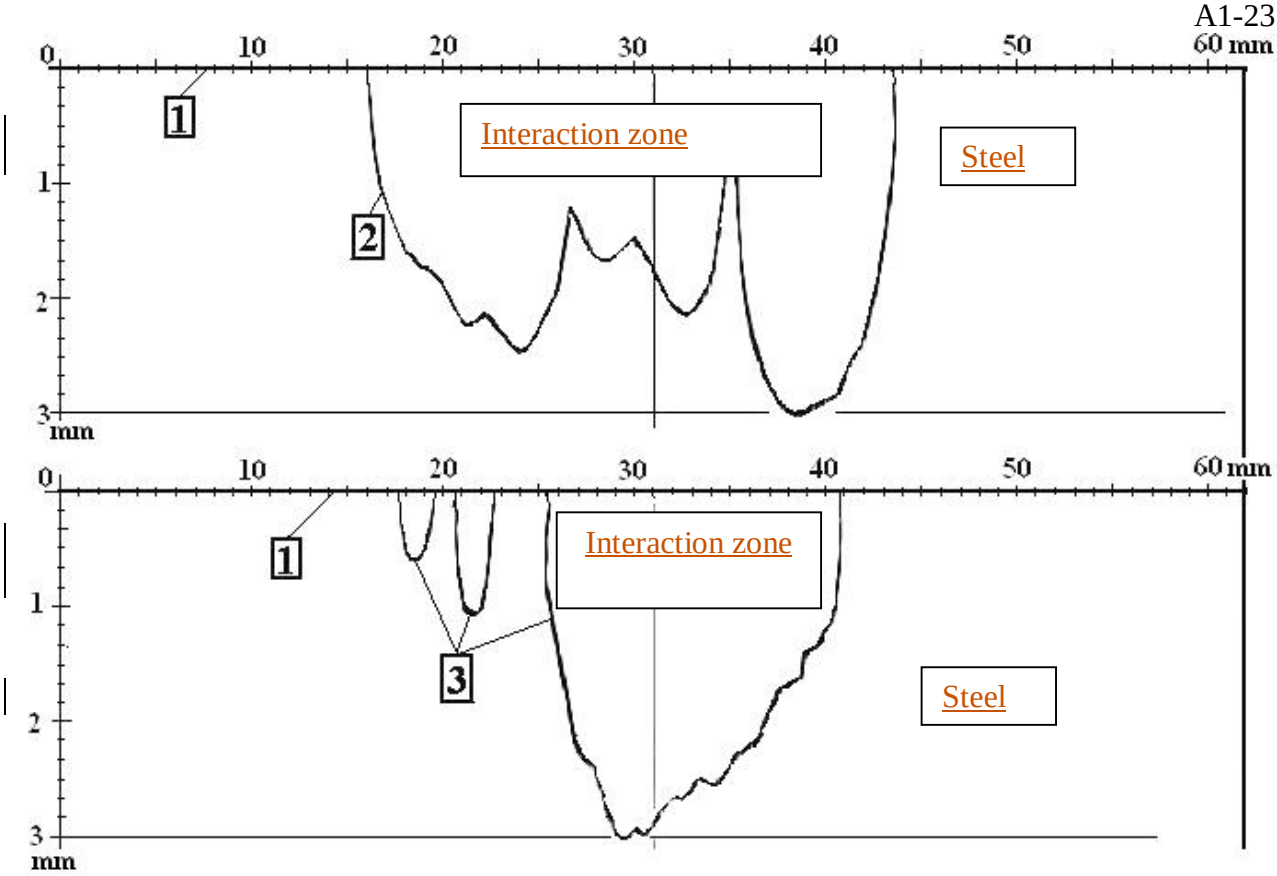

Fig. 2.6. Corium-steel interaction zone profilogram (micro-profile of the axial section of the steel specimen):

1 – initial position of the specimen top.
2 – profile of the corium-steel interaction zone in the A1-A2 section.
3 – profile of the corium-steel interaction zone in the section of Fig. 2.5 b.

Template grinding and polishing was carried out in accordance with standard methodology. In order to reveal the microstructure the prepared microsection was etched. The etchants for austenite and pearlite steels [6] were used, they enabled to reveal the macro- and microstructure of the corium-steel interaction zone and identify the microstructure of steel, which was subjected to the high temperature impact.

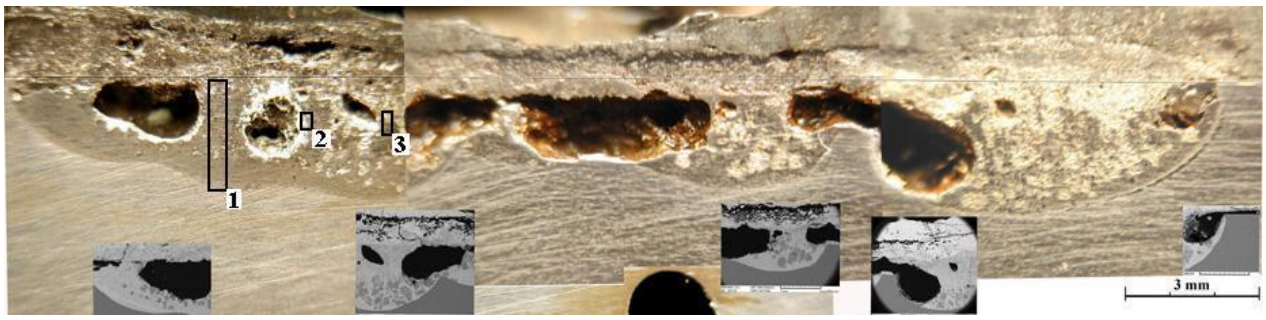

Fig. 2.7. A segment of corium-steel interaction macrosection with fragments of SEM images

The surface of sections was photographed by a digital camera "NIKON" through the metallographic microscope METALLUX with the magnification factor of 100; 200; 400 and 800.

After determining the macrostructure of the axial section (Fig. 28) a zone of thermal influence can be identified, that is the zone above line 3, which underwent the change of infrastructure. Fig. 29 shows the microstructures along the A-A line of Fig. 2.8, which were photographed after every 2-3 mm from the specimen top to line 3. Fig. 2.10 shows the microstructures along the axis and near the reference groove.

The temperature boundary of the structure-phase changes in the 15Kh2NMFA-A steel was identified by the metallographic studies and calculations of temperature distribution in the axial sections of the specimen top. The original microstructure is preserved below line 3.

Fig. 2.11 shows the modeled temperature distribution along the axis (Section 2.2), on which line 3 is drawn; it marks the boundary of molten corium influence on the steel macro- and micro-structure for the conditions of tests MC7 and MC6 [8]. The calculated temperature values have a satisfactory agreement with the temperature of 723°C, at which pearlite starts to transform into austenite in the steel having 0,12% of carbon (Ac_3) following iron-carbon diagram [6, 7].

The whole zone of steel between line 3 and the interaction boundary with disturbed structure can be defined as the zone of corium melt thermal impact. Its depth can be 15 mm. Its temperature range is 723 ÷ 1025 ^{o}C, and during the test it underwent changes from the initial ferrite-pearlite structure to the monophase austenite and back, which is similar to a conventional annealing procedure. During this the steel phase composition did not change, but the grain size did: it grew due to annealing. The lower part of the heat impact zone, Fig. 2.9 (e - f) went through the incomplete annealing in the 723 ÷ 850 ^{o}C range. The upper part, Fig 2.9 (c, d), - complete annealing in the 850 ÷ 950 ^{o}C range. The zone top, Fig. 2.9 (a, b), was subjected to the annealing with superheating, during which the grain grew up to ~ 500 µm. For this reason at cooling these grains disintegrated forming large ferrite grains, which, in their turn, got transformed at its decomposition due to the tertiary cementite liberation. Fragments in Fig 2.9 (a, b, c, f) are another evidence to it; they are located in the zone of complete high-temperature annealing with superheating.

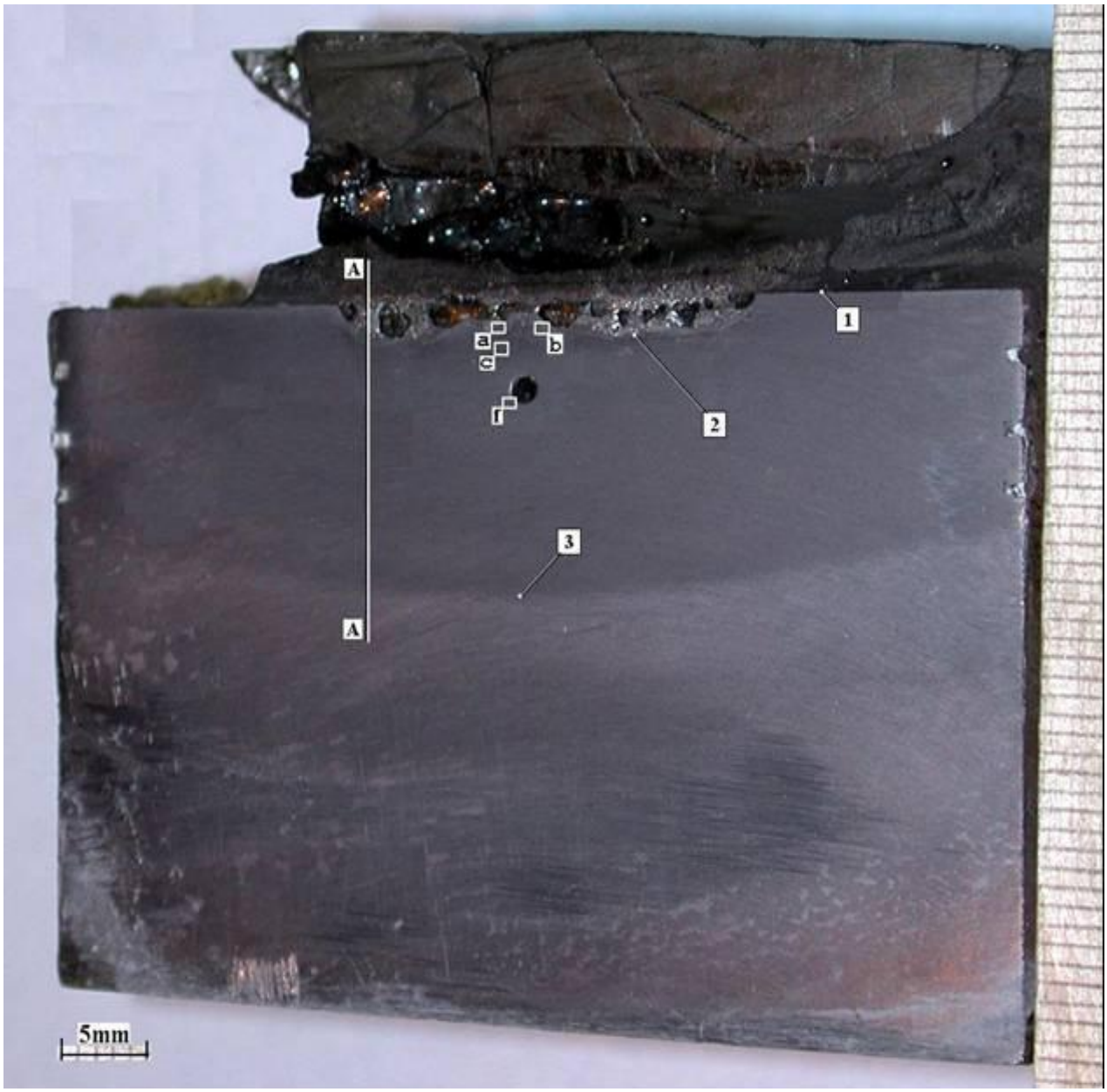

Fig. 2.8. Axial section of the steel specimen top:

1 – reference plane of the initial top;
2 – corium-steel interaction zone profile;
3 – boundary of the corium melt temperature influence on steel structure;
A-A – line, along which the microstructure was studied;
a - f – segments where the microstructure was studied.

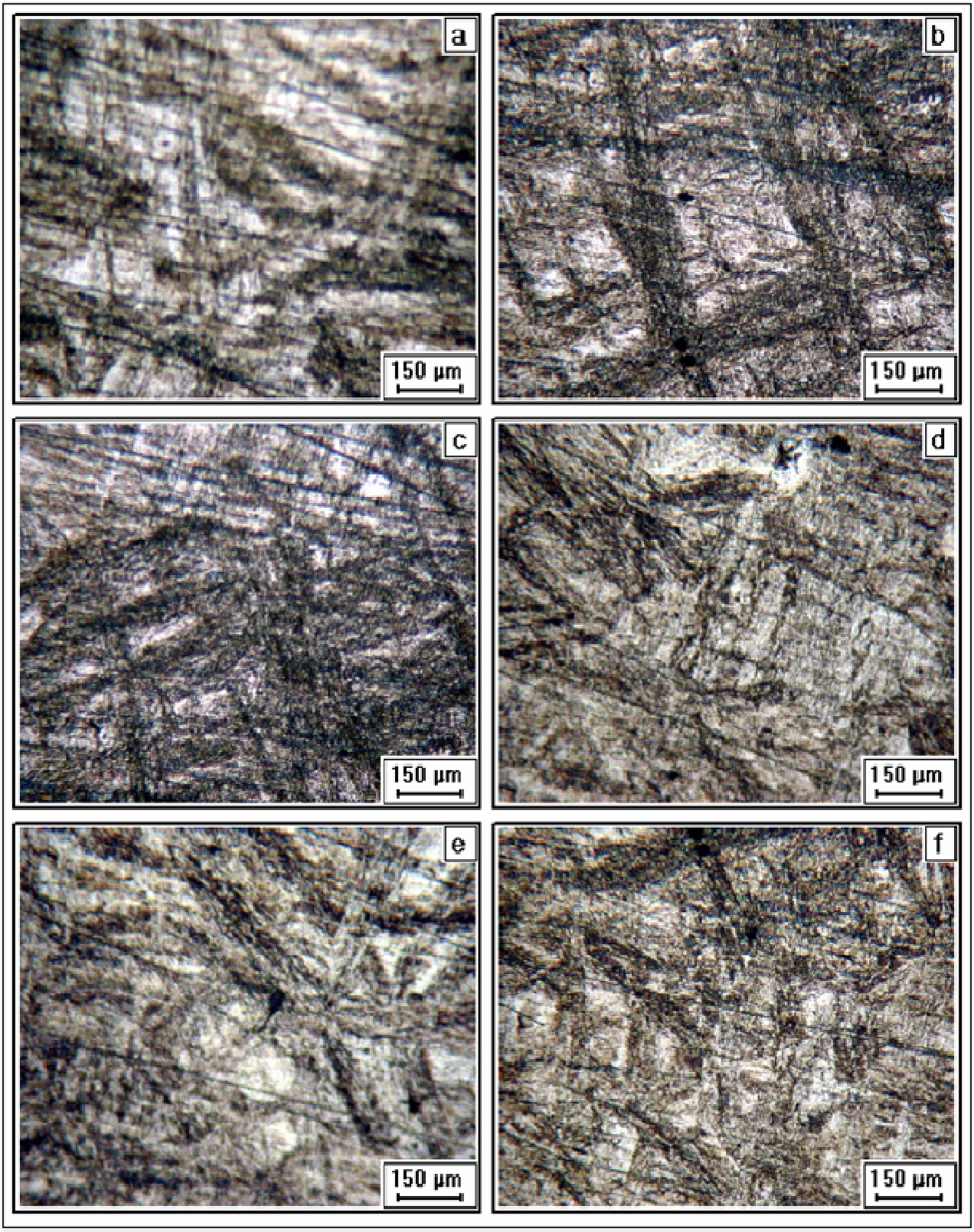

Fig. 2.9. Steel microstructure along the A-A line, Fig. 2.8

White and grey spots – ferrite (~90%)
Black spots – pearlite (~10%)

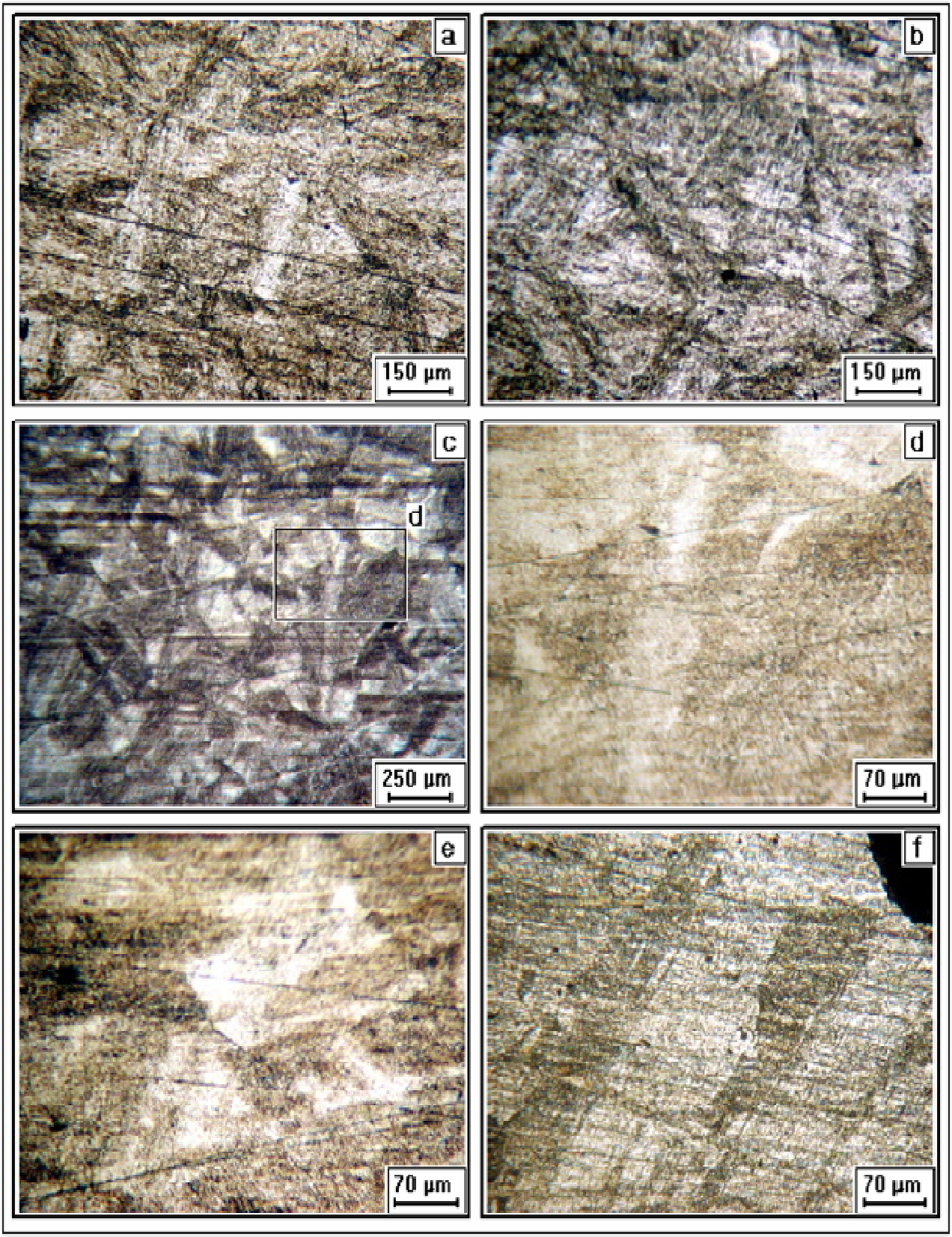

Fig. 2.10. Steel microstructure in the segments marked as a, b, c, f in Fig. 2.8

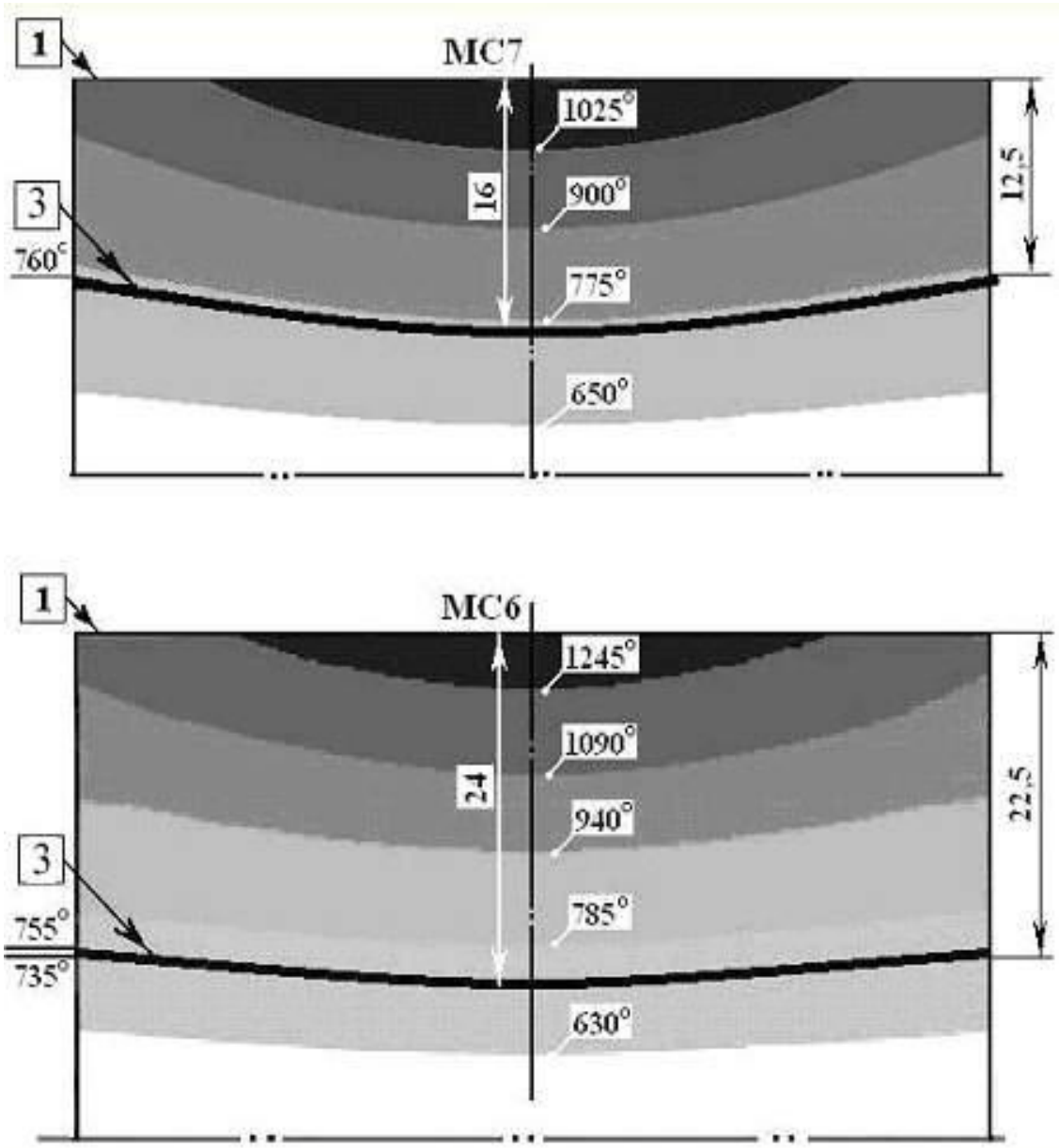

Fig. 2.11. Modeled temperature distribution in the steel specimen top:

1 – position of the initial top plane.

3 – boundary of the corium melt temperature influence on the steel macro- and micro-structure (Fig. 2.8).

2.3.2. SEM/EDX analysis of MC7 template

SEM analysis of microstructure and EDX analysis of corium elemental composition, interaction zone and steel specimen were performed on a single template, which was the axial section of the ingot. Figs. 2.12 - 2.22 and corresponding tables present the microstructures and elemental composition of segments chosen for studies. They are shown in Fig. 2.12.

The crystallized corium was examined far from the interaction zone (Fig. 2.12, segment 1). The analysis of microstructure revealed the presence of a distinct boundary, which separated the crystallized corium of the initial composition and microstructure with iron and chrome admixtures (Fig. 2.13, area SQ1), from the crust-adjacent zone, which was extensively enriched with uranium and where zirconium was depleted in comparison to initial corium, and which contained a prominent concentration of iron component (Fig. 2.13, SQ2). The microstructures of crystallized corium and crust-adjacent zone are quite different. After crystallization corium becomes a mixture of two phases: solid solution $U(Zr)O_2$ and α-Zr-based phase, containing a certain amount of UO_2 and FeO. The phase ratio is ~ 64 : 36 vol. %, respectively. The zone under corium contains at least four phases, and the α-Zr-based phase becomes smaller by one order in comparison to its content in the crystallized corium.

Interaction zone – the layer of specimen top next to the crust, which has undergone chemical and structural transformations**.** The zone microstructure is presented in Figs 2.14, 2.19, 2.20 and 2.21. Differently from test MC6 the MC7 interaction zone is shallower, below 3 mm, it has the uneven border with steel and rather large voids or pores with uneven walls. Their formation can be explained by the release of oxygen during the melt solidification or by the liberation of carbon dioxide produced during the oxidation of carbon diffused from steel. Shrinking could be mentioned as another possible cause of their formation.

Interaction zone has a microstructure typical of eutectic compositions. The EDX analysis of eutectics zones is given in Table 2.11, areas SQ1, SQ2 and SQ3 and in Fig. 2.16. Closeness of the three areas' compositions means that by 90% this zone is a multi-component eutectics. Only two phases could be identified in it: 1) phase having the composition of $U(Zr)Fe_2(O)$ (Fig. 2.15, point P1) and 2) α-Zr-based phase, containing some UO_2 and FeO (Fig. 2.15, point P2).

Beside the described eutectics the interaction zone has crystallized formations of tetragonal shape having the $Zr(U)Fe_4(O)$ composition (area SQ1, Fig. 2.14). They probably grew in the course of the test.

A nearly monophase layer of $U(Zr)Fe_2(O)$ crystals is found in the left part of the studied template, on the periphery of interaction zone near the boundary with steel (Fig. 2.14 – segments 2-1-3). The layer structure and crystal composition are given in Fig. 2.21, area SQ1 and in Table 2.12. This phase has been identified in the eutectics zone (Fig. 2.15, point P1). But it has not been found as a mono-crystal layer in other regions. The origin of this layer can be attributed to the peculiarities of melt crystallization in the interaction zone after the test. Once started, the crystallization had a high rate due to the heat transfer to steel. For this reason the initial (outer) structure of the layer is composed by many crystallites stretched in the direction opposite to the heat transfer vector and separated by the eutectics veins. During the layer formation the crystallization rate slowed down and crystallites formed a solid monophase growth front. This continued until the refractory phase $U(Zr)Fe_2(O)$ had crystallized completely, having shifted the melt composition to the eutectics. It was followed by the eutectics crystallization, Fig. 2.15.

The inter-grain diffusion of uranium and zirconium to the depth of ~ 10 μm is observed on the interface "interaction zone - steel" (Fig. 2.17, point P1). The studies of steel composition near the interaction zone (area SQ2, Fig. 2.17) and the initial one (Fig. 2.18 and Table 2.7) have not revealed any significant differences.

The analysis of microphotographs and phase composition around the crust layer testifies to a very inhomogeneous character of crystallization (Fig. 2.19 – regions 2-2-1 and 2-2-2, Fig. 2.20 – region 3-1, Fig. 2.13 – region 1-2, area SQ2). Near the interaction zone (Fig. 2.19– region 2-2-1) oxygen is depleted in the solidified melt; and five phases can be found in it (region 2-2-1, Fig. 2.19):

1) α-Zr-based phase, which contains a certain amount of UO_2 (point P1);
2) $Zr(U)Fe_2(O)$ phase with chrome admixture (point P2);
3) $U(Zr)Fe_2(O)$ phase with chrome admixture (point P3);
4) $U(Zr)O_2$ solid solution-based phase with iron admixture (point P4);
5) U_5FeO_2 phase (point P5).

The fuzziness of "interaction zone-crust" boundary should be noted. The crystallization pattern in this region is shown in microphotographs (Figs. 2.14 , 2.19 - 2.22). The presence of longitudinally crystallized parts and a considerable deviation of the boundary from the isotherm surface indicate that the interaction in the test did not reach the steady-state stage.

The concentration of uranium near the boundary "crust-interaction zone" and "crust-crystallized corium" is on the level of 72 mass%. In the zone maximally saturated with oxygen (Fig. 2.21) the concentration of uranium is 79 mass%.

The transport of zirconium takes place in parallel with the uranium transfer. Its concentration varies from 11 mass % in region 1-2, (Fig. 2.13) to 3-4 mass% near the interaction zone.

Oxygen concentration changes from 11,7 mass% in the crystallized corium (Fig. 2.14, area SQ2) to 14 mass%, i.e. stoichiometry, in region 3 (Fig. 2.20, segments 3-1).

In parallel with U, Zr and O diffusion into steel an *outdiffusion* of iron and its alloying components into corium is observed. As far as 0.5 mm from the interaction zone a drop of iron concentration in corium from 14 mass% to 3.5 mass% is found.

The concentration of chrome gradually decreases from the interaction zone to crystallized corium from 1.0 to 0.5 mass%.

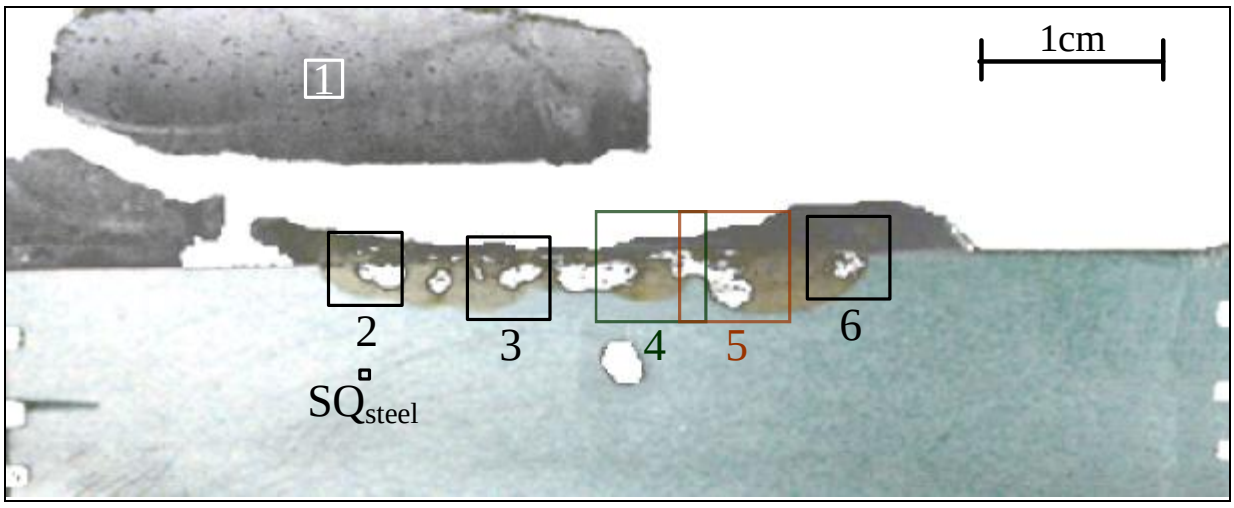

Fig. 2.12. MC7 template with studied segments

Table 2.8

EDX analysis of steel

№		Fe	Cr	Ni	Mn	Si
SQ_{steel} (0.5×0.5 mm)	mass%	95.08	2.33	1.48	0.6	0.5
	mole%	94.51	2.49	1.4	0.61	1

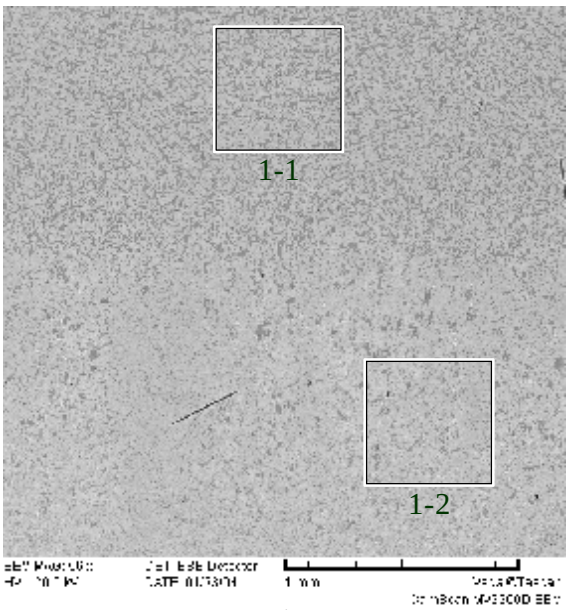

1

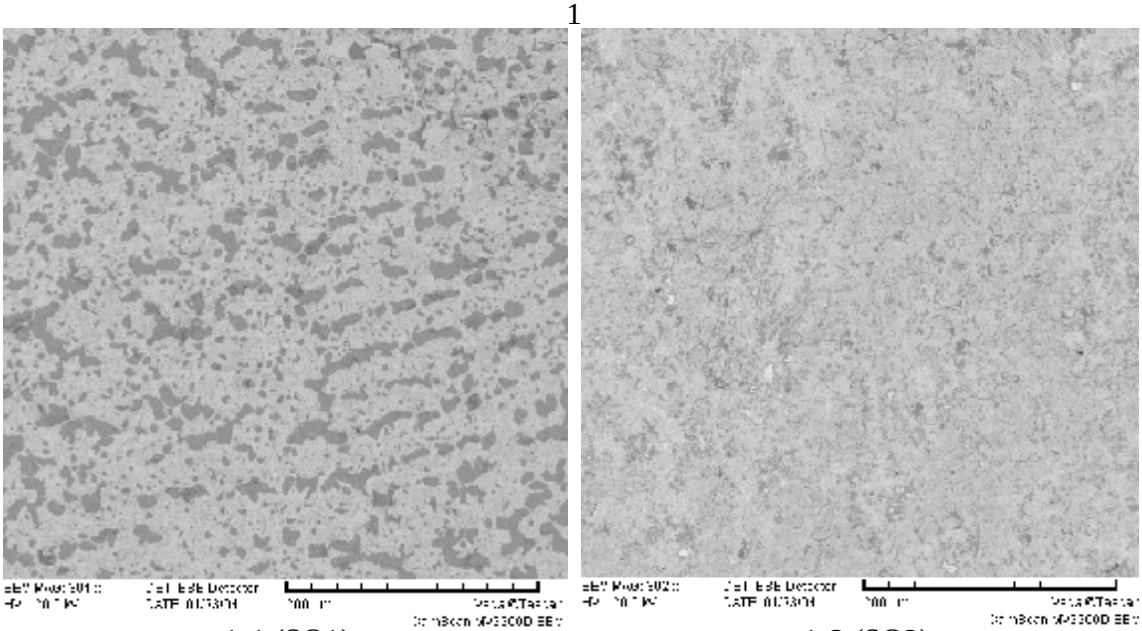

1-1 (SQ1) 1-2 (SQ2)

Fig. 2.13. Microphotograph of Segment 1 (crystallized corium)

Table 2.9

EDX analysis of Segment 1

№		U	Zr	Fe	Cr	Ni	Th	O
SQ1 (0.4×0.4 mm)	mass%	57.2	29.8	0.47	0.48	-	-	12.05
	mole%	17.96	24.42	0.63	0.7	-	-	56.29

SQ2 (0.4×0.4 mm)	mass%	72.29	10.98	3.51	0.48	-	1.05	11.69
	mole%	24.66	9.77	5.11	0.74	-	0.37	59.35

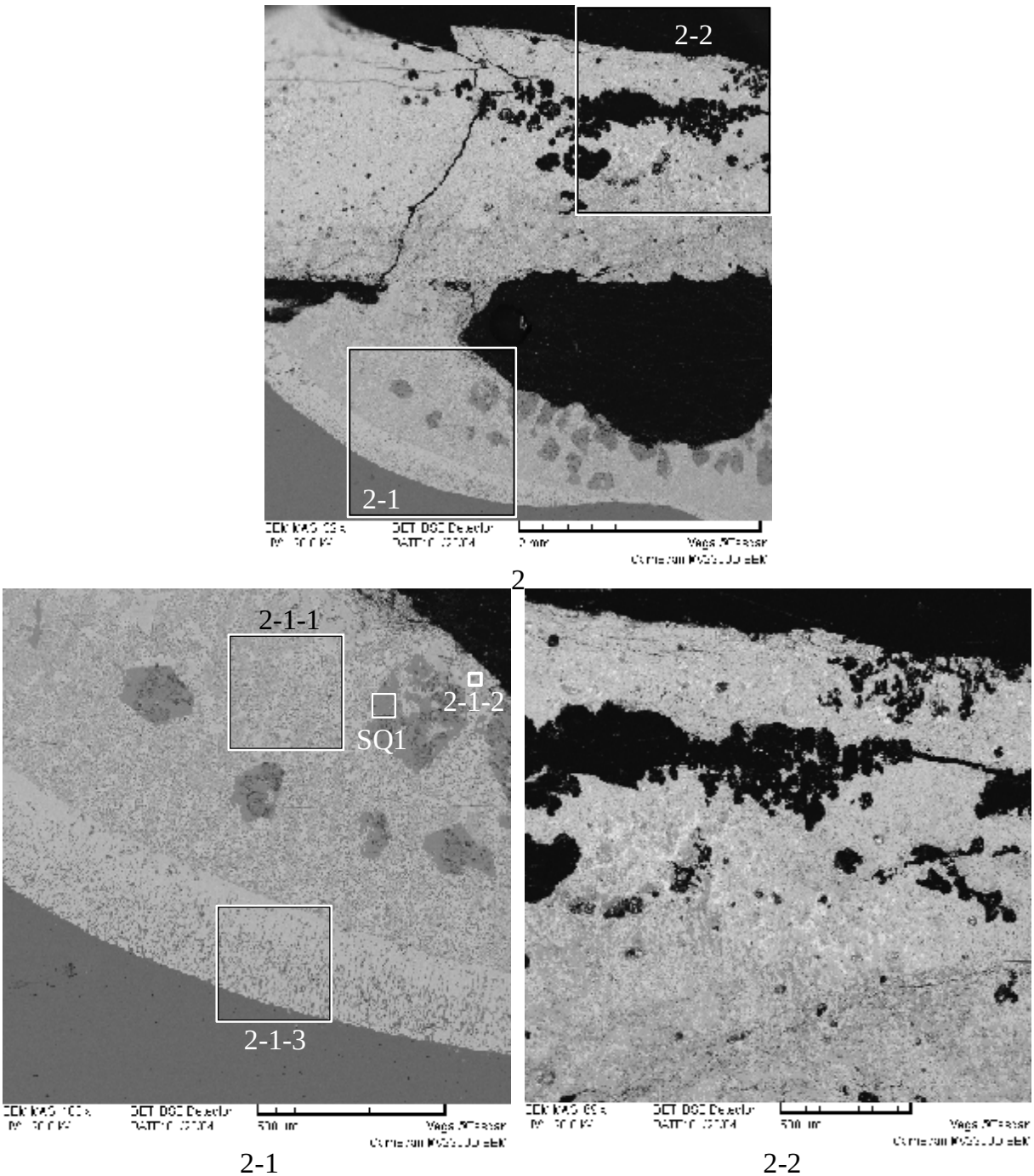

Fig. 2.14. Microphotograph of Segment 2 (interaction zone)

Table 2.10

EDX analysis of Segment 2

№		U	Zr	Fe	Cr	Ni	Si	O
SQ1 (0.1×0.1 mm)	mass%	11.59	22.47	62.3	1.69	0.54	0.8	0.62
	mole%	3.2	16.21	73.43	2.13	0.6	1.87	2.55

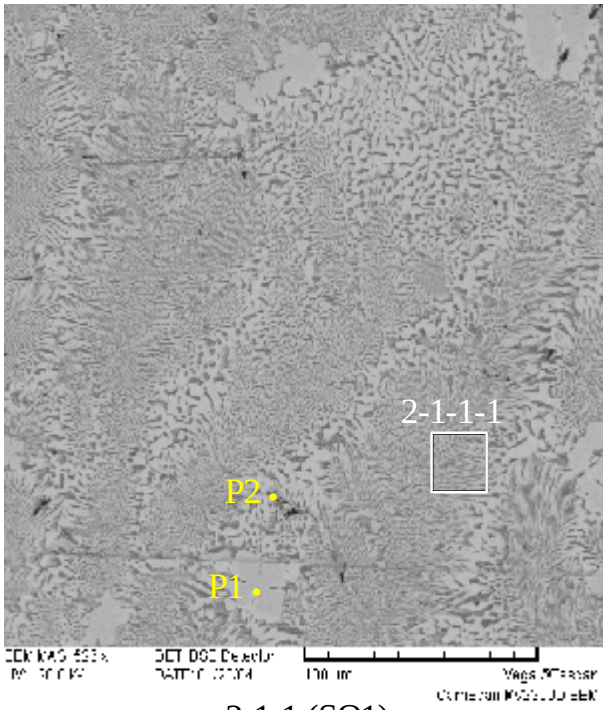

2-1-1 (SQ1)

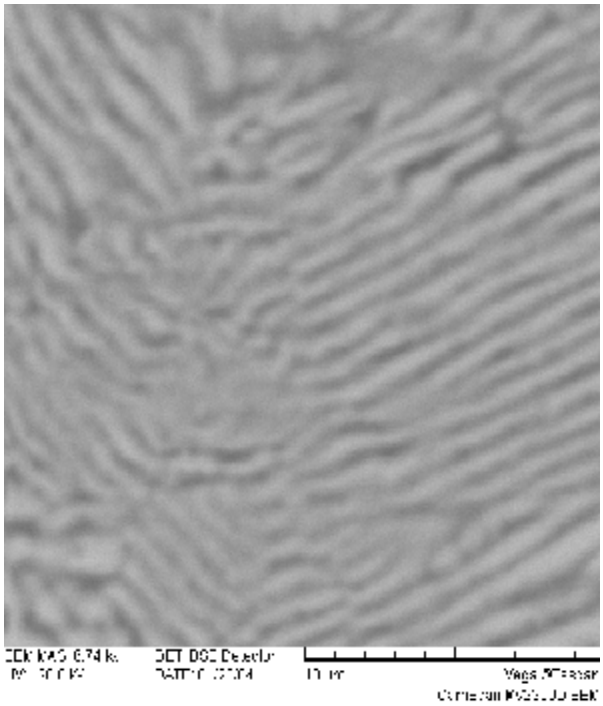

2-1-1-1 (SQ2)

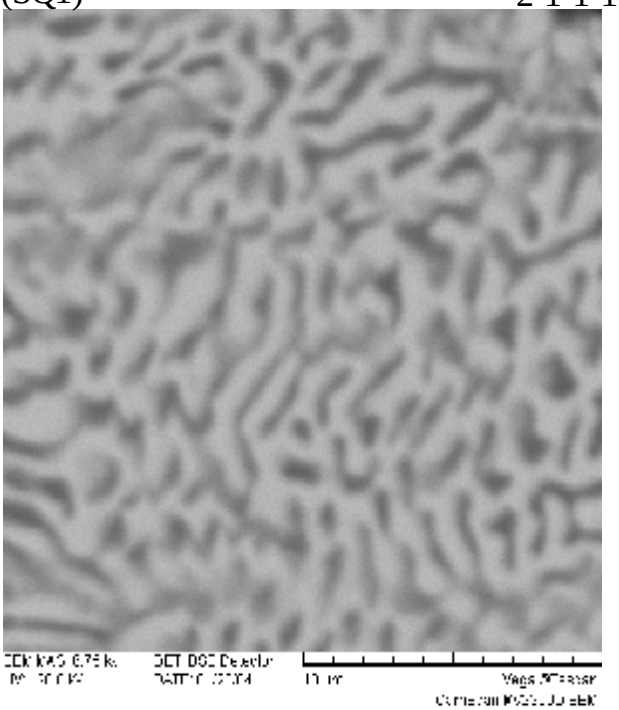

2-1-2 (SQ3)

Fig. 2.15. Microphotographs of segments 2-1-1 and 2-1-2 (eutectics region of the interaction zone)

Table 2.11.

EDX analysis of segments 2-1-1 and 2-1-2

№		U	Zr	Fe	Cr	Ni	Mn	Si	O
SQ1 (0.2×0.2 mm)	mass%	43.95	2.15	49.63	1.58	0.72	0.45	0.4	1.11
	mole%	14.99	1.91	72.16	2.46	0.99	0.67	1.15	5.65
SQ2 (20×20 µm)	mass%	40.35	2.26	53.44	1.66	0.78	-	-	1.51
	mole%	13.13	1.92	74.12	2.47	1.04	-	-	7.33
SQ3 (20×20 µm)	mass%	41.35	2.25	52.48	1.71	0.6	0.58	-	1.03
	mole%	13.83	1.96	74.82	2.61	0.82	0.84	-	5.12
P1	mass%	55.38	4.83	37.05	-	0.84	-	0.44	1.46
	mole%	21.74	4.95	62	-	1.33	-	1.47	8.51
P2	mass%	2.01	93.25	1.31	-	-	-	-	3.44
	mole%	0.66	80.57	1.84	-	-	-	-	16.92

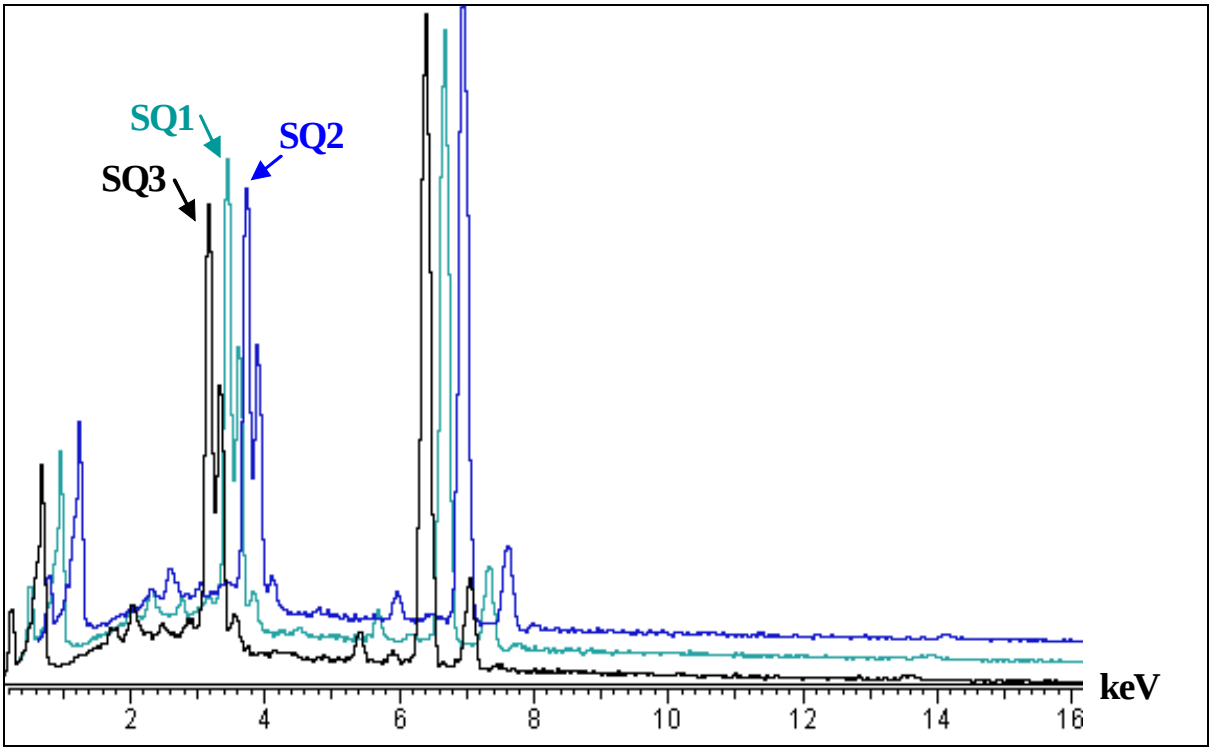

Fig. 2.16. Comparison of the eutectics zones spectra from segments 2-1-1 and 2-1-2

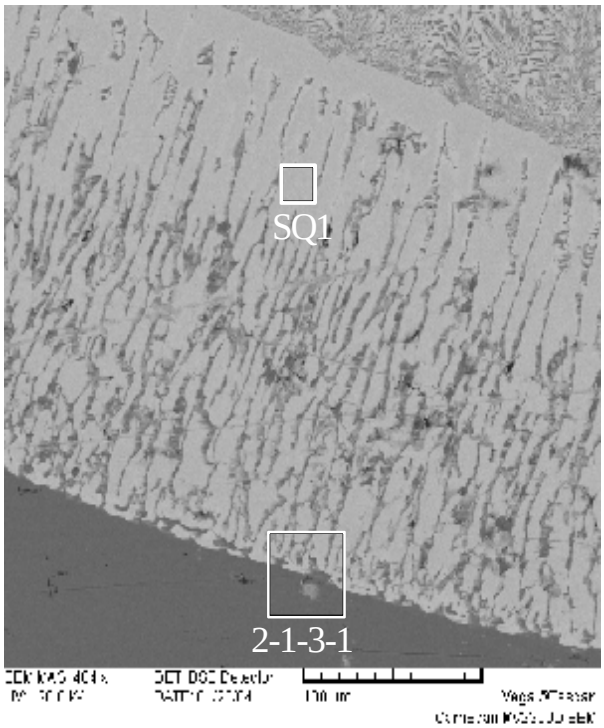

2-1-3

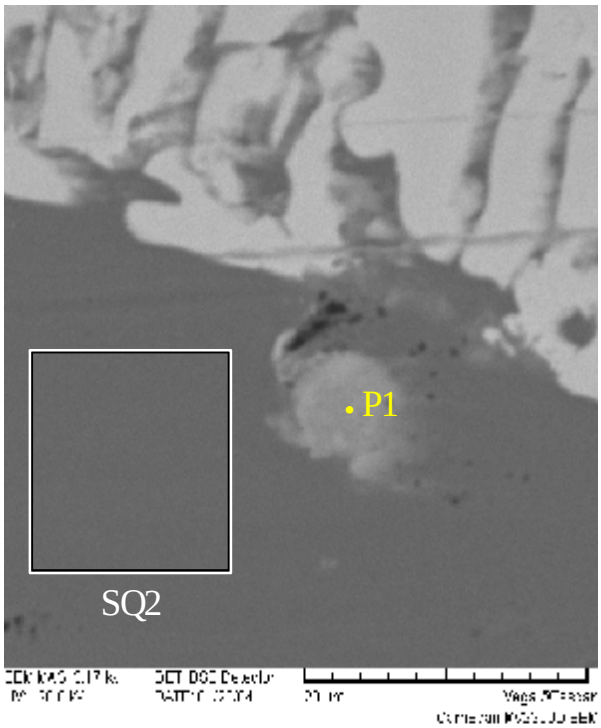

2-1-3-1

Fig. 2.17. Microphotograph of Segment 2-1-3 (boundary between the interaction zone and steel)

Table 2.12

EDX analysis of segments 2-1-1 and 2-1-2

№		U	Zr	Fe	Cr	Ni	Mn	Si	O
SQ1 (20×20 μm)	mass%	54.89	4.48	37.48	0.5	0.79	-	-	1.85
	mole%	21.16	4.51	61.6	0.88	1.24	-	-	10.61
SQ2 (10×10 μm)	mass%	-	-	96.2	2.2	1.13	-	0.46	-
	mole%	-	-	95.66	2.35	1.07	-	0.91	-
P1	mass%	28.3	2.93	64.32	2.59	0.6	0.51	-	0.75
	mole%	8.38	2.26	81.16	3.51	0.72	0.66	-	3.32

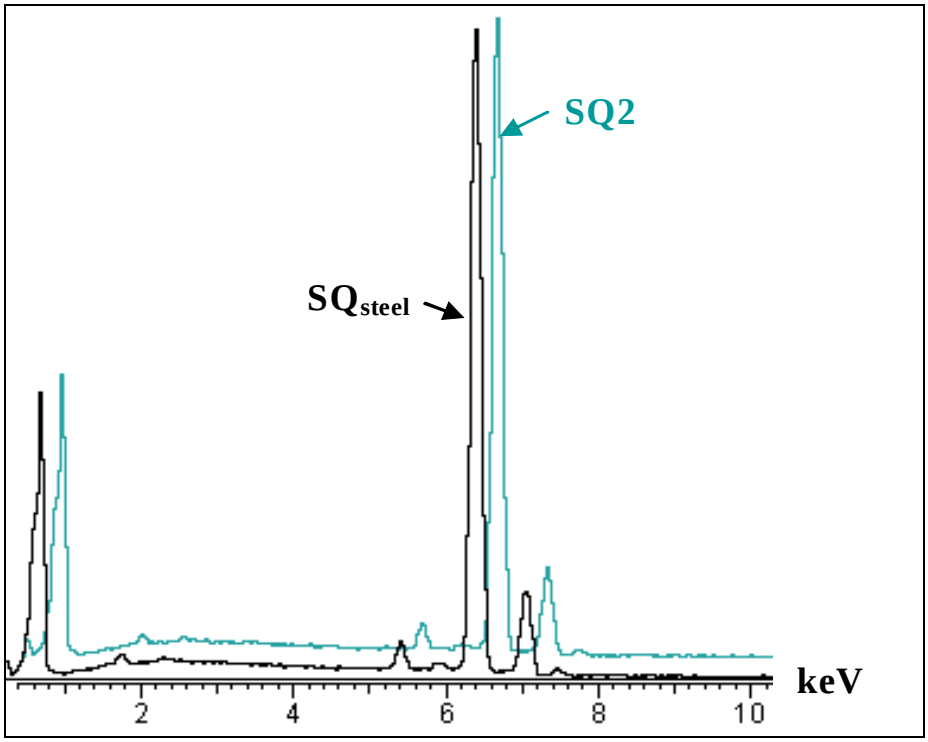

Fig. 2.18. Comparison of the spectra of pure steel and steel near the diffusion zone

Table 2.13

Comparison of the EDX analysis data of pure steel and steel near the diffusion zone

№		Fe	Cr	Ni	Mn	Si
SQ_{steel} (0.5×0.5 mm)	mass%	95.08	2.33	1.48	0.6	0.5
	mole%	94.51	2.49	1.4	0.61	1
SQ2 (10×10 μm)	mass%	96.2	2.2	1.13	-	0.46
	mole%	95.66	2.35	1.07	-	0.91

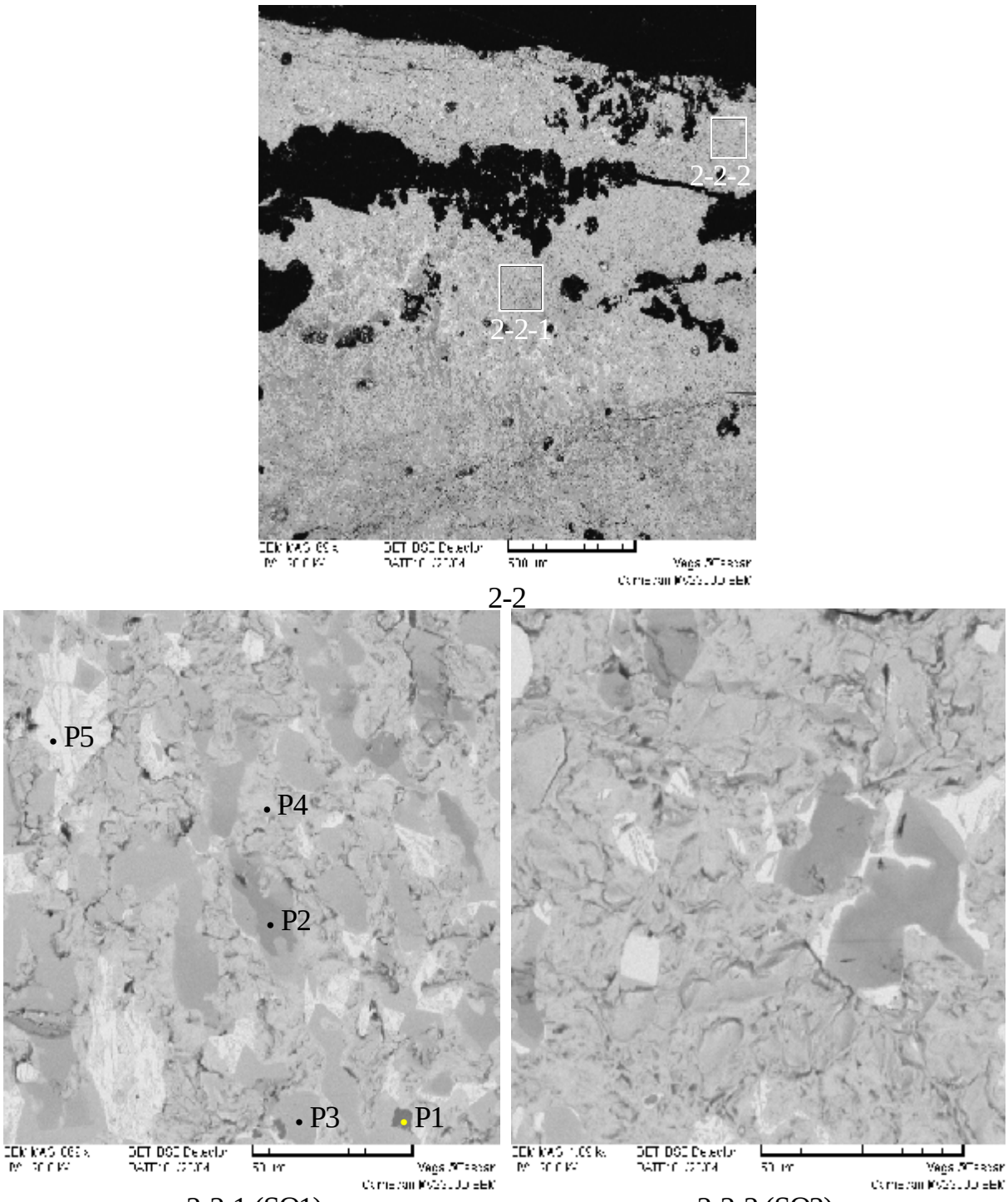

Fig. 2.19. Microphotographs of segments 2-2 (interaction zone – corium boundary)

Table 2.14

EDX analysis of Segment 2-2

№		U	Zr	Fe	Cr	Th	O
SQ1	mass%	71.93	3.42	14.2	1.08	-	9.37
(0.1×0.1 mm)	mole%	25.18	3.12	21.19	1.74	-	48.78
SQ2	mass%	74.47	3.95	7.28	0.81	0.99	12.51
(0.1×0.1 mm)	mole%	24.29	3.36	10.12	1.2	0.33	60.7
P1	mass%	2.73	93.14	-	-	-	4.13
	mole%	0.89	79.11	-	-	-	20
P2	mass%	29.22	24.44	43.81	1.64	-	0.89
	mole%	9.72	21.23	62.15	2.51	-	4.39
P3	mass%	52.56	9.42	35.63	1.15	-	1.24
	mole%	20.8	9.72	60.09	2.09	-	7.31
P4	mass%	86.84	1.09	0.68	-	-	11.39
	mole%	33.14	1.09	1.1	-	-	64.67
P5	mass%	93.37	-	4.22	-	-	2.41
	mole%	63.41	-	12.21	-	-	24.38

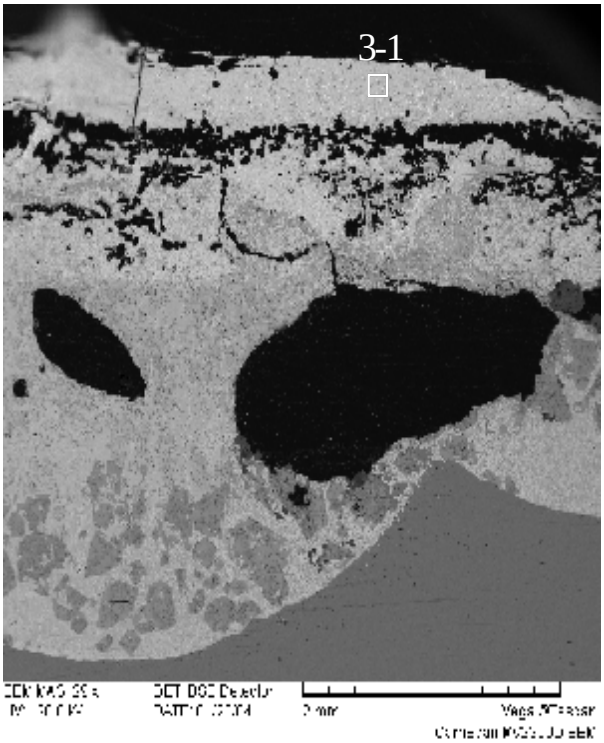

3

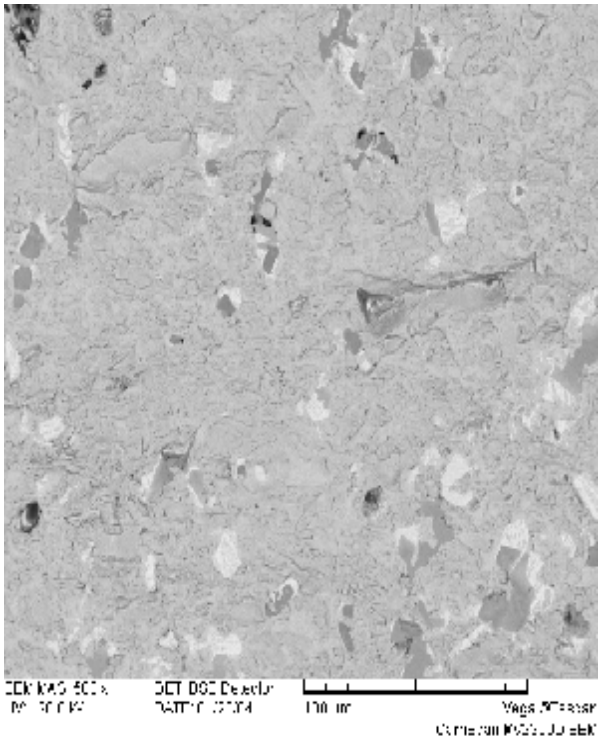

3-1 (SQ1)

Fig. 2.20. Microphotographs of Segment 3

Table 2.15.

EDX analysis of Segment 3

№		U	Zr	Fe	Cr	O
SQ1 (0.2×0.2 mm)	mass%	78.96	3.06	3.39	0.56	14.03
	mole %	25.26	2.56	4.62	0.82	66.76

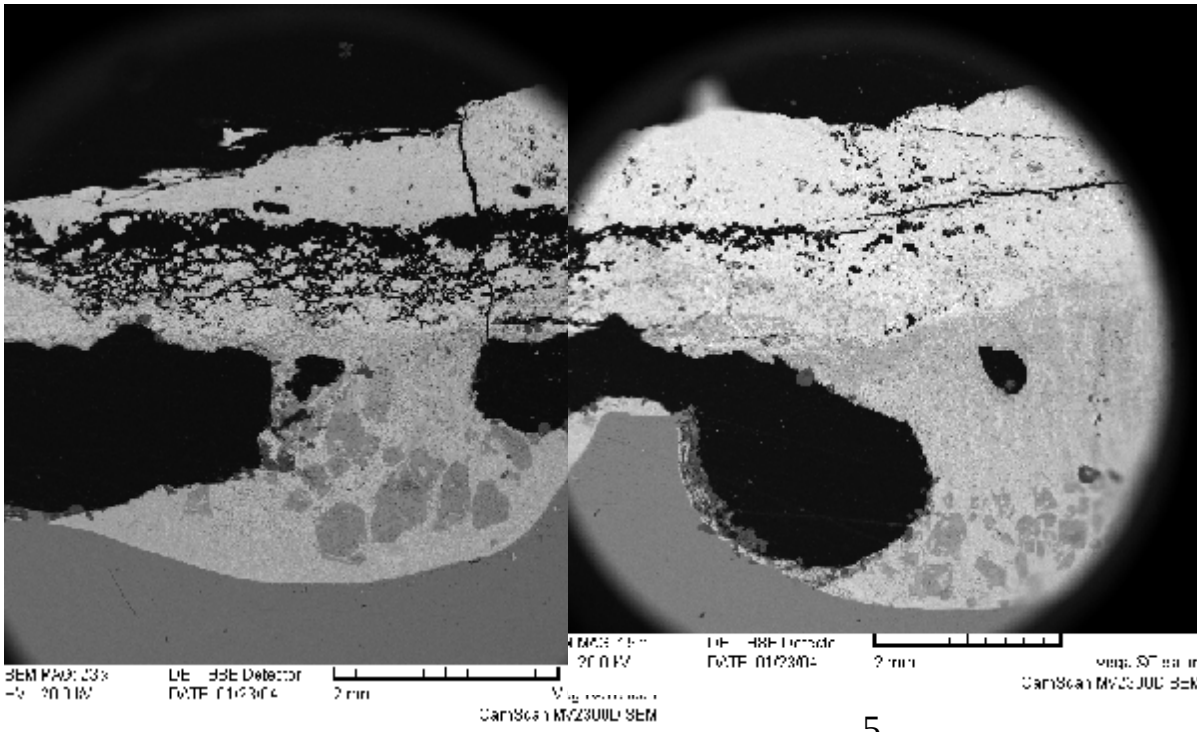

4 5

Fig. 2.21. Microphotographs of segments 4 and 5

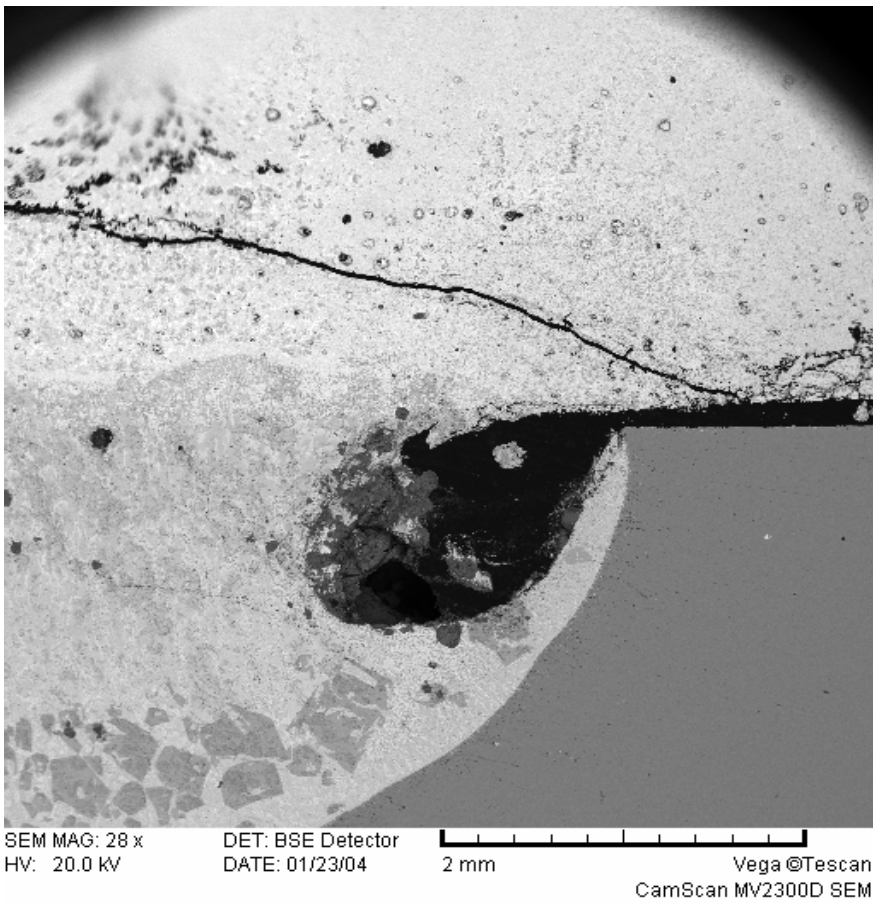

Fig. 2.22. Microphotograph of Segment 6

2.3.3. Differential thermal analysis

The differential thermal analysis (DTA) of samples taken from the steel – corium C-32 interaction zone in tests MC6 and MC7 was made by the SETSYS Evolution-2400 analyzer. SETSOFT 2000 software was used for the processing of results.

The temperature of steel-corium interaction start (solidus temperature) was indicated by the start of endothermic effect at the sample heating and by the start of exothermic effect at its cooling, the second was somewhat lower than the first. The difference in the solidus temperature values is explained by a possible sample subcooling below the solidus temperature during cooling, whereas there has not been detected any substantial superheating of the solid state above the solidus point in numerous tests performed by us. Therefore we consider the value registered at heating as more credible .

The DTA conditions:

The mass of samples was ≈ 6 mg, the experimental section was sparged with helium at the 4 ml/min flow rate, the heating rate was 5^{o}C/nin; B-type thermocouples were used (Pt-30%Pt/Rh - 6% Rh). Tables 2.16 (Fig. 2.23) and 2.17 (Fig 2.15) give the eutectics composition in the samples for tests MC6 and MC7, they were taken for the DTA using the data of SEM/EDX analysis.

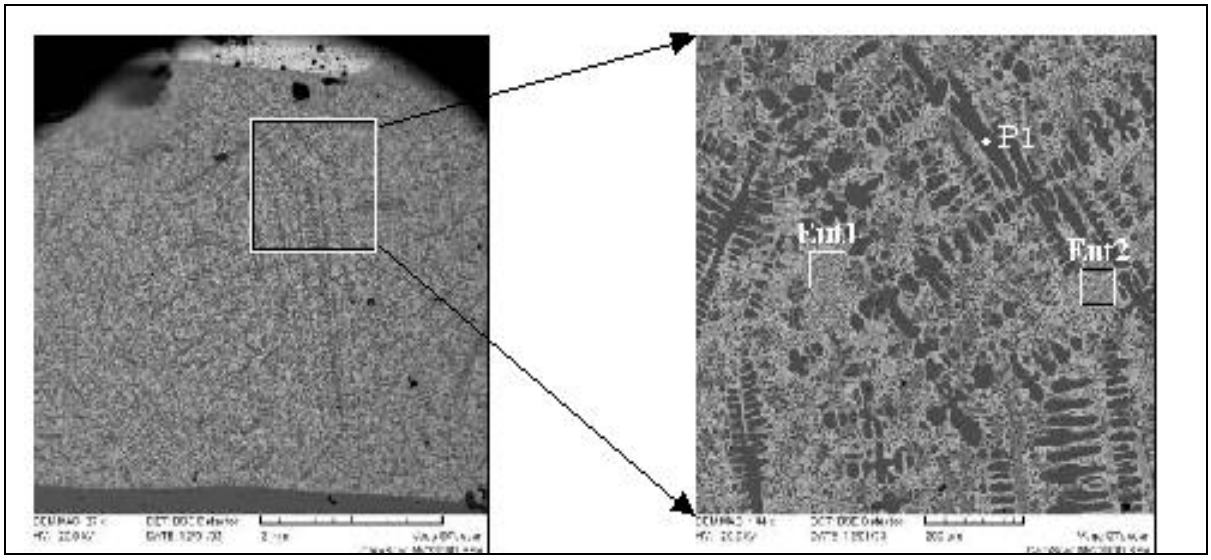

Fig. 2.23. Microstructure of the MC6 interaction region

Table 2.16

Eutectics composition in the MC6 sample in accordance with SEM/EDX.

Sample	U	Zr	Fe	Cr	Ni	O
	Mass%					
Eut1	38.5	1.0	56.5	1.2	1.2	1.5
Eut2	37.9	1.2	56.8	1.2	1.1	1.6

Table 2.17

EDX analysis of segments 2-1-1 and 2-1-2 (MC7)

№		U	Zr	Fe	Cr	Ni	Mn	Ni	O
Eut	mass%	40.35	2.26	53.44	1.66	0.78	-	-	1.51

Figs. 2.24-2.27 show DTA curves of MC6 and MC7 samples.

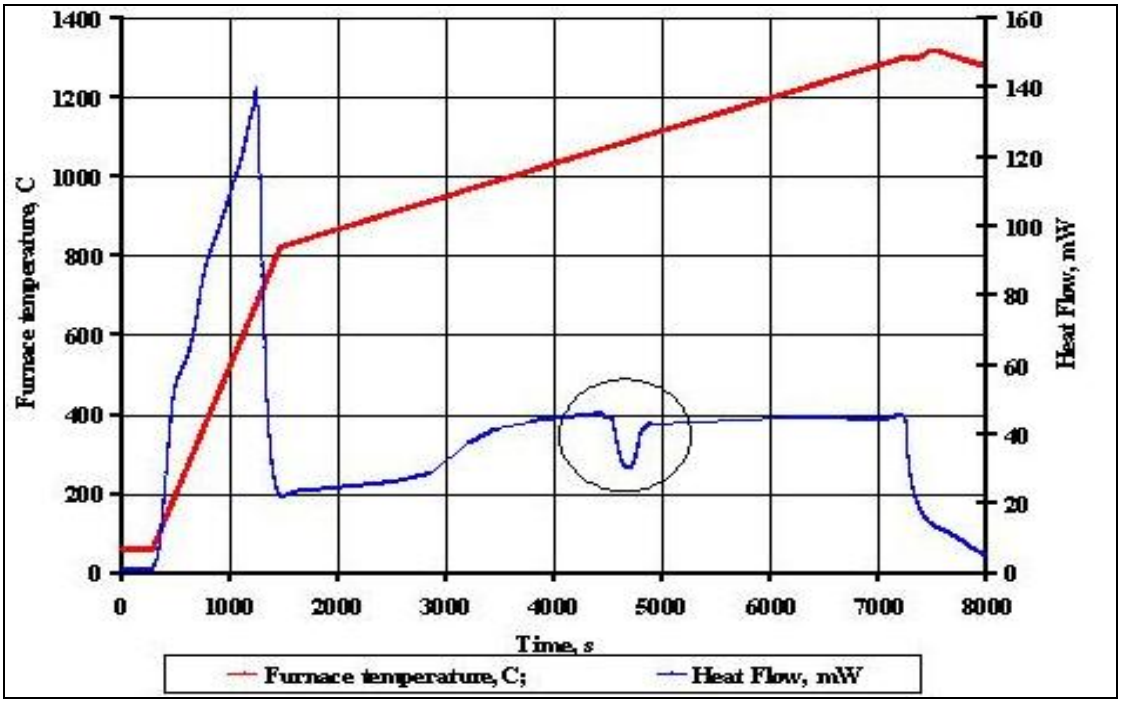

Fig. 2.24. DTA curve during the MC6 sample heating

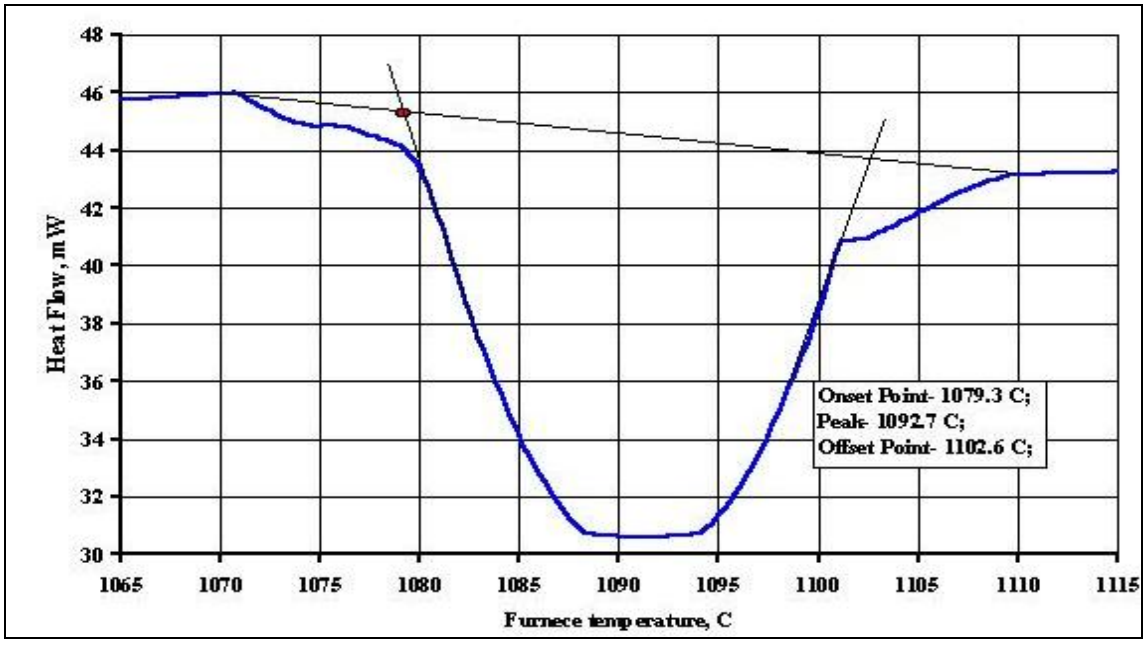

Fig. 2.25. Enlarged part of Fig. 2.24

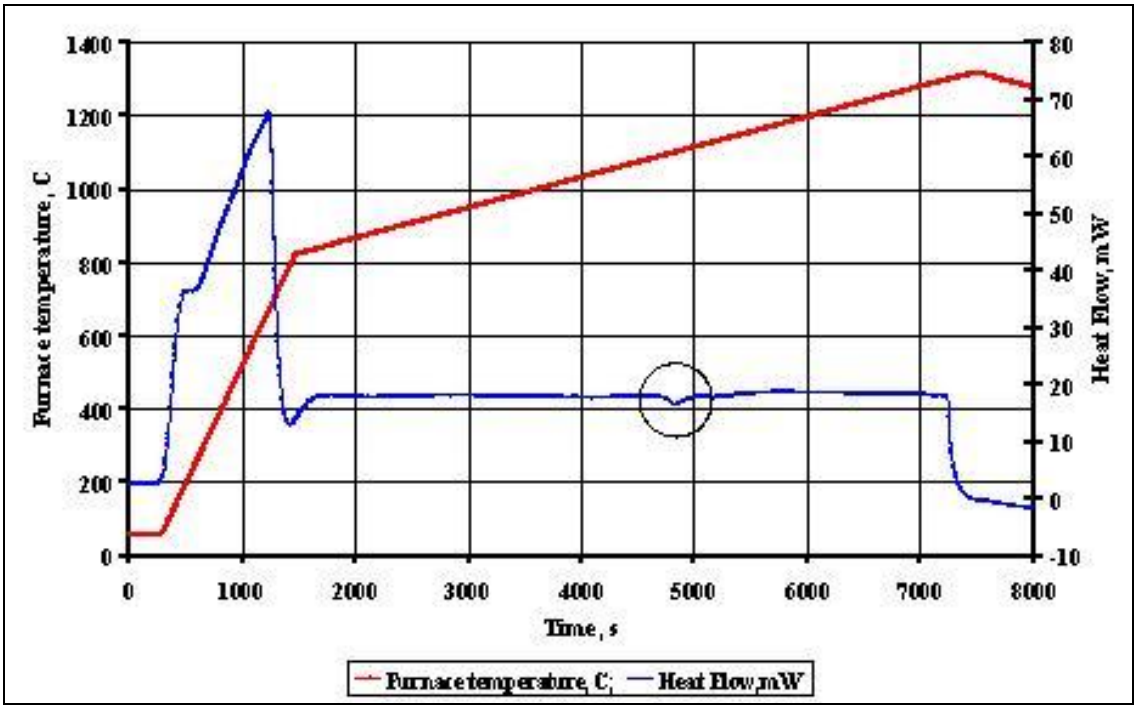

Fig. 2.26. DTA curve during the MC7 sample heating

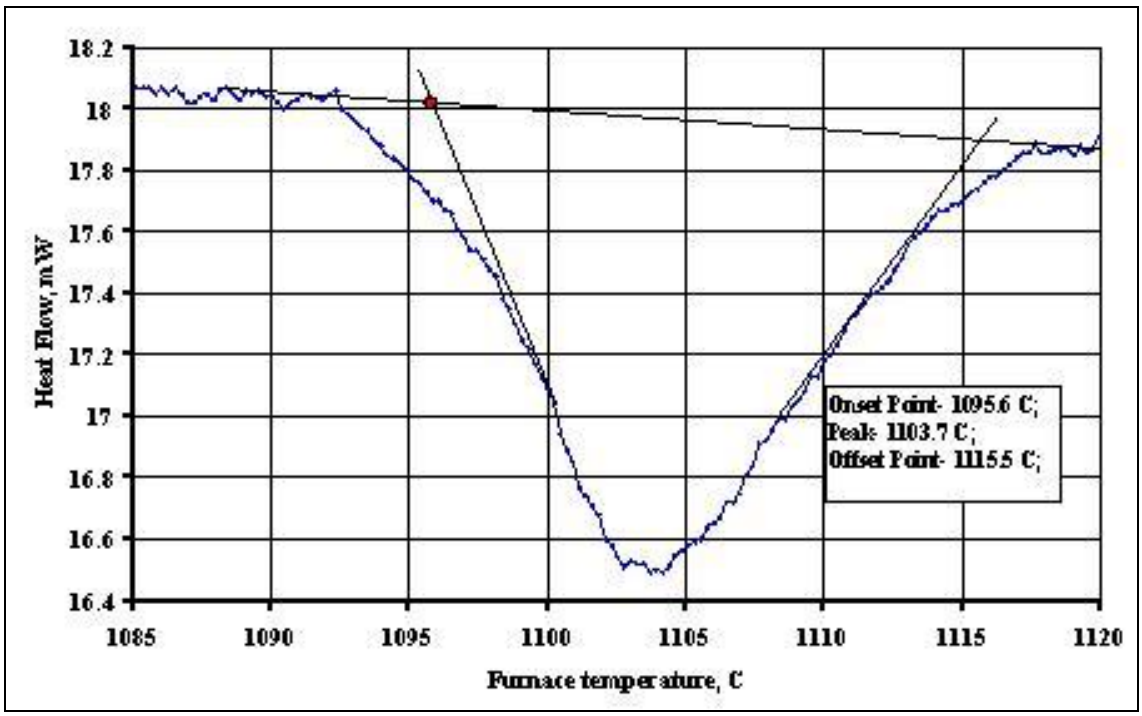

Fig. 2.27. Enlarged fragment of Fig. 2.26

Figs. 2.25 and 2.27 demonstrate distinct peaks with endothermic effect between 1079 - 1103°C for MC6 and between 1097 - 1116°C for MC7. In order to determined the temperature corresponding to the peak start the baseline "linear from first to last point" was chosen, after which tangent lines to the peak slopes were drawn. The intersection of base and tangent lines was on the temperature level corresponding to the solidus temperature of 1079°C (MC6) and 1096°C (MC7).

A small divergence of temperatures can be attributed to the error of DTA measurements and explained by minor differences in the composition of multicomponent eutectics in different tests (Table 2.3.7-2.3.8).

2.4. Ultrasonic measurements of the specimen ablation rate

Just like in the previous tests the objective of MC7 ultrasonic (US) measurements was to determine the kinetics of the corium-steel interaction boundary progress.

The methodology for measurements and data processing was explained in detail in the MC5 and MC6 reports.

Test MC7 was started with the following values of the main parameters (Table 2.18).

Table 2.18

Initial values of main parameters

Parameter	Notation	Value	Unit	Note
Total specimen length	$L_{gen.}$	102.41	mm	
Distance between the defect and the first measurement point	l_1	0.085	mm	6.00 mm from the top
Distance between the defect and the second measurement point	l_2	4,085	mm	2.00 mm from the top
Initial distance between the defect and top	D_o	6.085	mm	
Initial speed of sound in the specimen	C	5.84	km/s.	

β value determined in the test was $1{,}9 \cdot 10^{-4}$ $(^{o}C)^{-1}$. Coefficient $b = \frac{C_0 - C(T)}{TC(T)}$.

Figs. 2.28, 2.29, 2.30 give the essential data of US measurements and results of their processing.

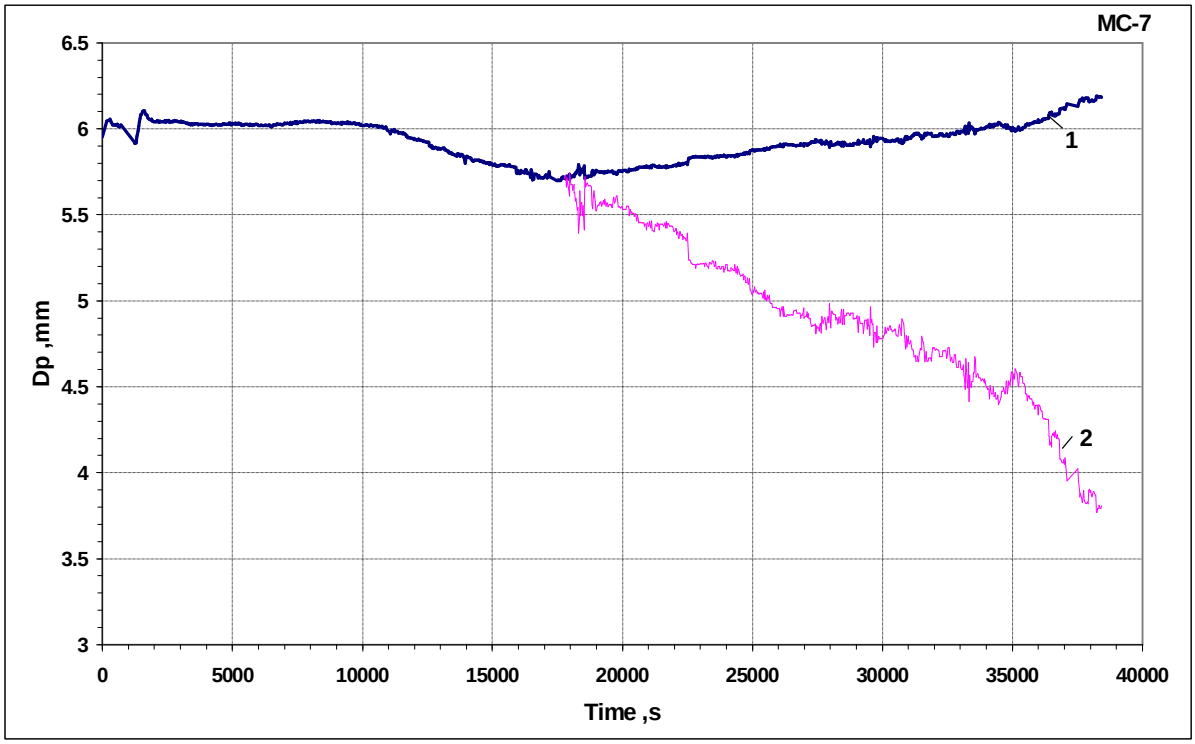

Fig. 2.28. Plot of distance change between the top and acoustic defect {Dp(t)} during the time of observations (Curve 1) and the interaction lower boundary position {Dp(18000)-H(t)} (Curve 2) (evaluation from Dp(t) using ratio (1) (MC6 Report [8])

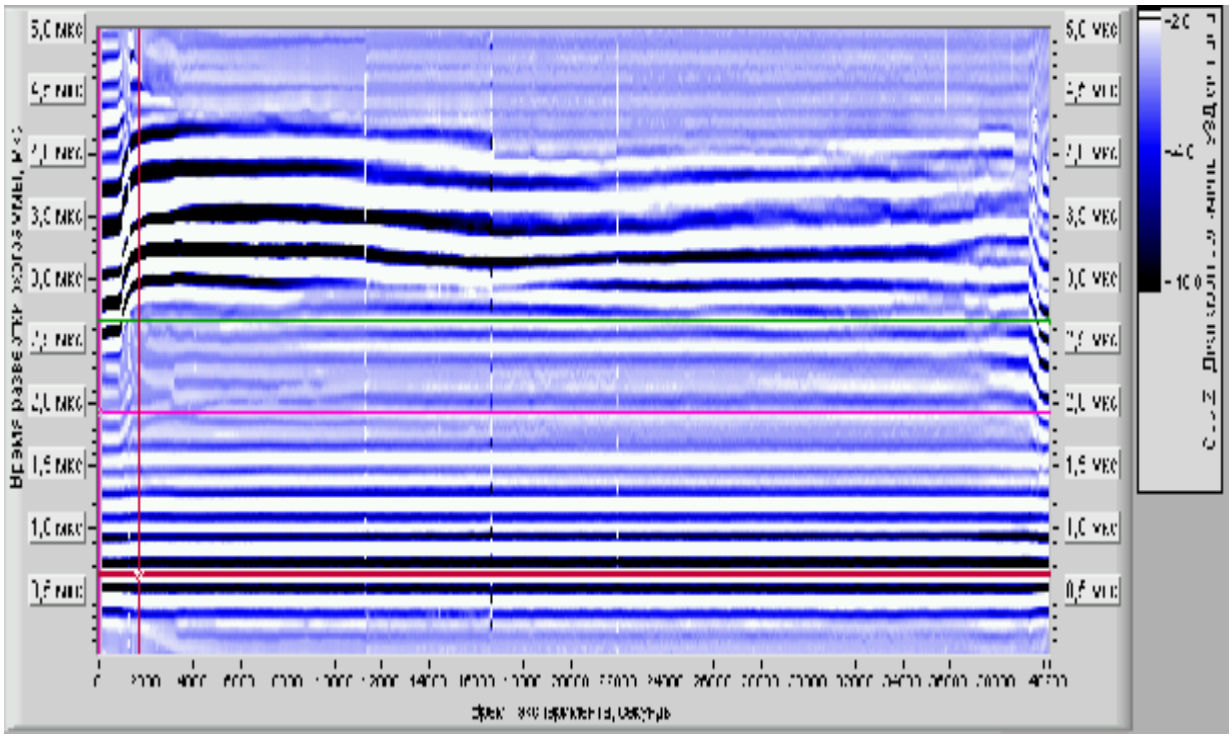

Fig. 2.29. Echogram field of the process; the signal level is in the range of -2 - -8 relative units

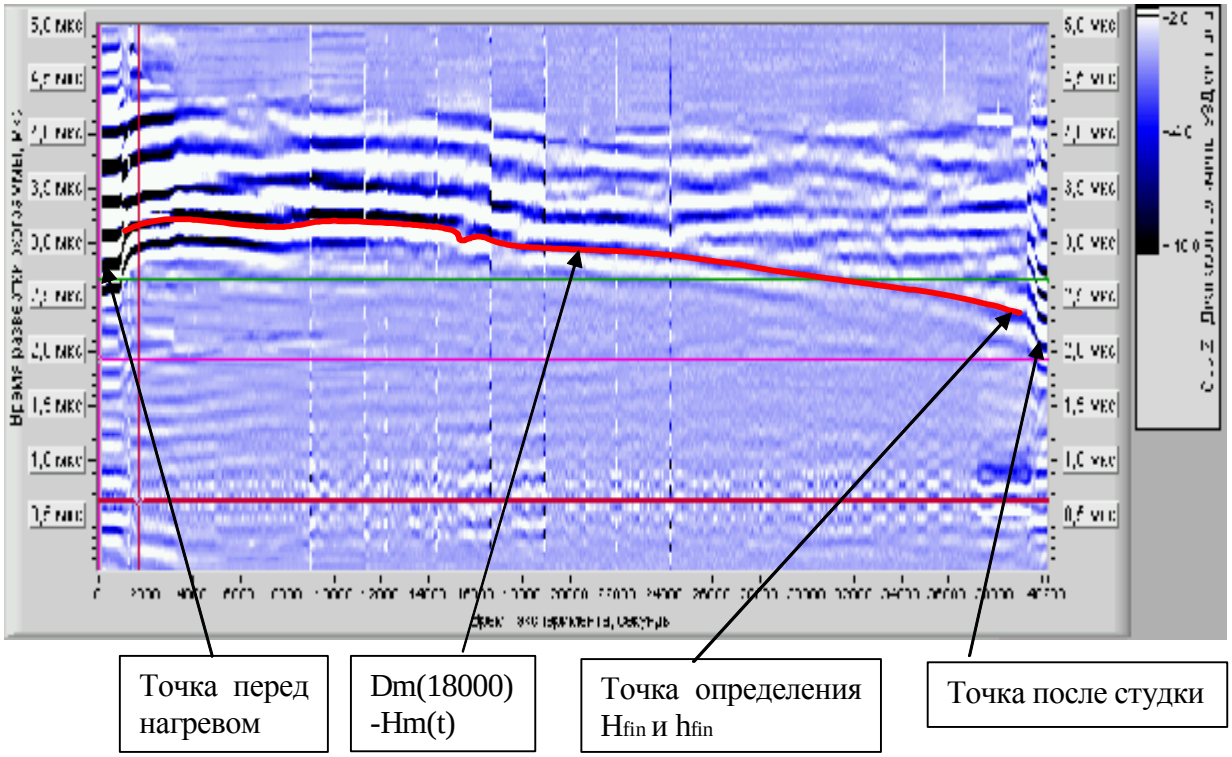

Point before heating **Point of H_{fin} and h_{fin} determination** **Point after cooling**

Fig. 2.30. Echogram field of the interaction after processing by subtraction. The plot of lower interaction boundary position change {$D_m(18000)-H_m(t)$}. Index m denotes the measured value without the temperature amendment

The echogram scanning time **τ** is the ratio of changed distances:

$$Dm_1 - Dm_2 = 0.5C_0(t_1 - t_2)$$

The actual distance Dp is derived from Dm by introducing temperature amendment:

$$D_p = \frac{C(T)}{C_o} D_m$$

As it is evident from Fig. 2.28 (Curve 1), a slow distance reduction between the specimen top and defect is observed between the process start (approximately the 11000th second of the test) and the 18000th second. The distance is shortened by ~ 0,2 mm, the value which testifies to the corrosion of specimen in contact with corium. Later, starting from ~ the 18000th second and up to the moment of power disconnection $D_p(t)$ was gradually increased by ~ 0,5 mm. In difference to MC6, the MC7 $D_p(t)$ curve is not saturated. Like in MC6 the apparent growth of $D_p(t)$ is explained not by the actual specimen lengthening, but by the slower speed of sound in the *interaction zone*, which gets saturated with Zr and U, changes its phase condition and, correspondingly, acoustic characteristics.

Starting from the 18000th second (Fig. 2.30) a signal is observed, which moves from the top to the defect. We interpret the signal as a reflection from the lower interaction boundary. The position of this signal at the time of heating disconnection denotes the final depth of the interaction zone (Fig 2.30). The distance, which the signal reflected from the interaction boundary passed between the 18000th s. and the time of heating disconnection, has been determined using the data of Fig. 2.30 taking into account the temperature amendment. It is H_{fin} = 2.1 mm, (Fig. 2.28).

Further, following the considerations explained in the MC6 Report we can estimate the character of lower interaction boundary H(t) progress from $h(t) = D_p(t) - D(18000)$

$$H(t) = h(t)\frac{H_{fin}}{h_{fin}},$$

where, H_{fin} = 2.1 mm, h_{fin} = 0.5 mm.

The resulting curve H(t) is shown in Fig. 2.30.

As it is seen from Fig. 2.30, the evaluation of H(t) using (1) has a good agreement with the position of signal reflected from the lower interaction boundary.

In contrast to MC6 the posttest analysis of MC7 sample has shown that the final position of the lower interaction boundary has a noticeable irregularity. The MC7 boundary is a surface, which has local depth maximums. The maximums near the specimen axis are 2- 3 mm deep (Fig. 2.6).

This is likely to cause the interference of signals from maximums and result in an average value of the interaction zone depth. The final depth determined from the US measurements, calculated from the initial position of the specimen top H_{fin} + Dp(0) – Dp(18000) = 2.3 mm lies within the mentioned distance and, in our opinion, proves a good agreement of the US and posttest measurements of the interaction boundary profilogram.

The applied technique of US measurements cannot be used for measuring the progression rate of the separate maximums.

In conclusion the following should be mentioned:

At the early stage, between 11000 - 18000 seconds, the corrosion of MC7 specimen is observed. Its rate is $2{,}86 \times 10^{-5}$ mm/s.

Starting from the 18000^{th} s. the US measurements indicate the formation of *interaction zone* and its propagation into the specimen bulk. *The interaction zone* started to form after ~ 5,5 hours from the experiment start.

Differently from MC6, in which after a certain period of time H(t) saturation was observed, the propagation of the *interaction zone* into the MC7 specimen bulk continues at an approximately constant rate, $1{,}0 \times 10^{-4}$ mm/s.

3. Discussion of results

3.1. Comparison of indicative zones in the MC6 and MC7 templates

In both experiments ~ C-30 corium compositions were used, and the exposure time was 10 hours. The main difference between MC7 and MC6: MC7 temperature on the corium-steel boundary, T_s ~ 1150ºC, and in MC6 - T_s ~1400ºC.

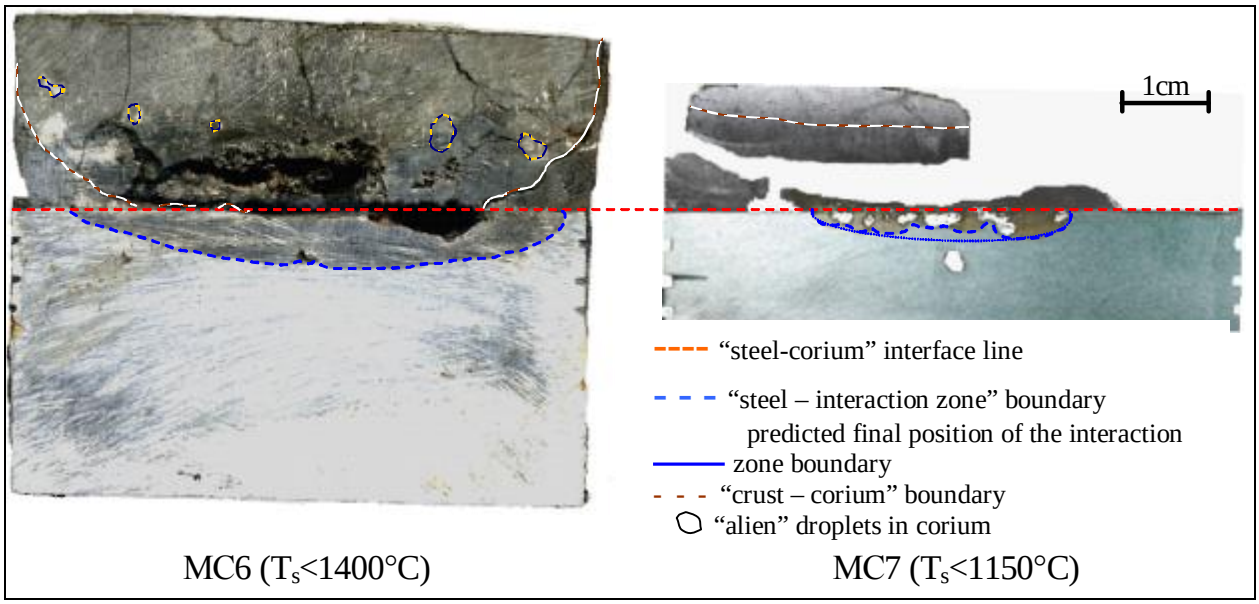

Fig. 3.1. MC6 and MC7 ingot cross-sections

Fig. 3.1. shows the photographs of the diameter sections of the MC6 and MC7 ingots

The visual and SEM/EDX analyses has shown the following:

- Both ingots have a region of degenerated steel (*interaction zone*).

- In the MC6 ingot the *interaction zone* is located asymmetrically to the ingot center; the boundary with steel is smooth and corresponds to the 1120 ... 1200 ^{o}C isotherm in the specimen.

- In the MC7 ingot the *interaction zone* boundary with steel has an uneven surface. In accordance with the US data it can be explained by a too short corium-steel interaction period. Steel temperature in the predicted final position of the boundary is lower than in MC6, it is 1030 ... 1100 ^{o}C.

- *The interaction zone* in MC6 ingot looks solid and nonporous, and the similar MC7 zone has large pores. The MC6 ingot has a large porous layer between the *interaction zone* and crystallized corium, and the MC7 ingot does not demonstrate such strong porosity above the zone.

- The SEM/EDX analysis of the interaction zone has revealed that in case of MC6 it is a crystallized dendrite-type homogeneous melt. And in case of MC-7 it is a melt, which is very close to eutectics, and we observe the crystallization pattern typical of the eutectics compositions.

- Foreign inclusions are observed in the corium part of the MC6 ingot. The SEM/EDX analysis of those inclusions has demonstrated that they are crystallized melt droplets from the interaction zone, which got transported into corium due to a break of the thin crust. There is

nothing like this in the MC7 ingot. The absence of suchlike inclusions in the MC7 ingot can be explained by a thicker crust, which does not break in the given experimental conditions.

Fig. 3.2. presents microphotographs for the comparison of the *interaction zone* crystallization pattern of MC6 and MC7. In the MC6 ingot the *interaction zone* is enriched with iron, which crystallizes as dendrites at melt cooling (Point P1, Fig. 3.2). In the *interaction zone* of the MC7 ingot a phase having similar or close composition is not observed. The melt, which in MC6 crystallized between dendrites, has a eutectic character.

In MC7 the SEM/EDX analysis has not been efficient in determining the average composition of the interaction zone due to its strong inhomogeneity caused by the uneven distribution of $Zr(U)Fe_2(O)$ phase, high porosity, broken boundary and the $U(Zr)Fe_2(O)$ layer, which formed near it. But it can be stated that compared to MC6 iron is depleted and it is enriched with U and Zr. If the difference of densities between the phases is neglected, we can give a rough estimate of the average composition from the difference of areas occupied by the eutectics and other phases. Eutectics occupies about 80 vol.% of the *interaction zone*.

The presence of pores in the MC7 interaction zone can be explained by the difference of this test from the experimental conditions of MC6: much lower temperature on the top boundary of the zone and, consequently, lower average temperature in the zone itself. In MC7 the difference is explained by a smaller heat flux from the melt. A higher temperature gradient and lower heat flux on the top of the MC7 interaction zone explains the presence of a thicker crust on it. After heating is disconnected, the interaction zone cooling starts from the specimen side. In MC7 the crystallization of this zone goes faster than in MC6 due to its originally lower temperature and better insulation from corium. It can be assumed, that in the MC7 conditions there is no time for the gas, which is liberated at the interaction zone cooling and crystallization, to be released into corium and it forms the observed pores.

The eutectics compositions of MC6 and MC7 are close (Fig. 3.2 and Table 3.1, Eut1 – Eut3).

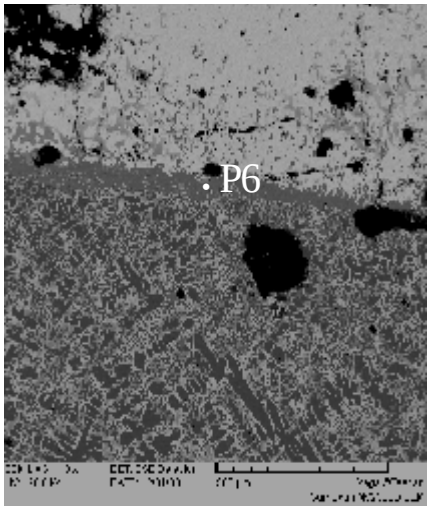

MC6

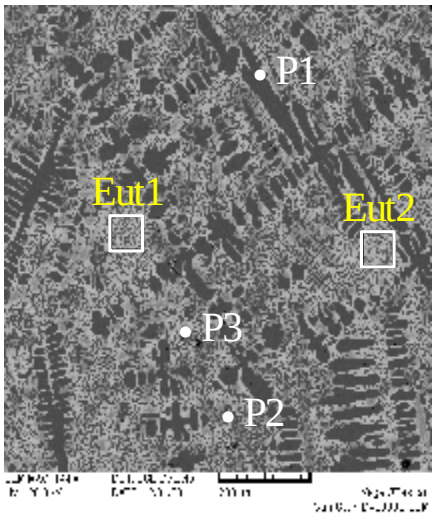

MC6 (SQ1)

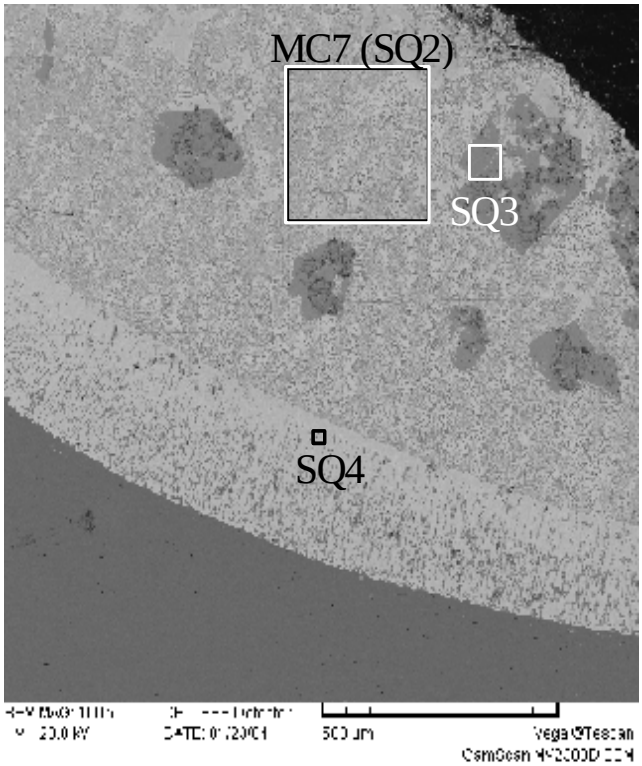

MC7

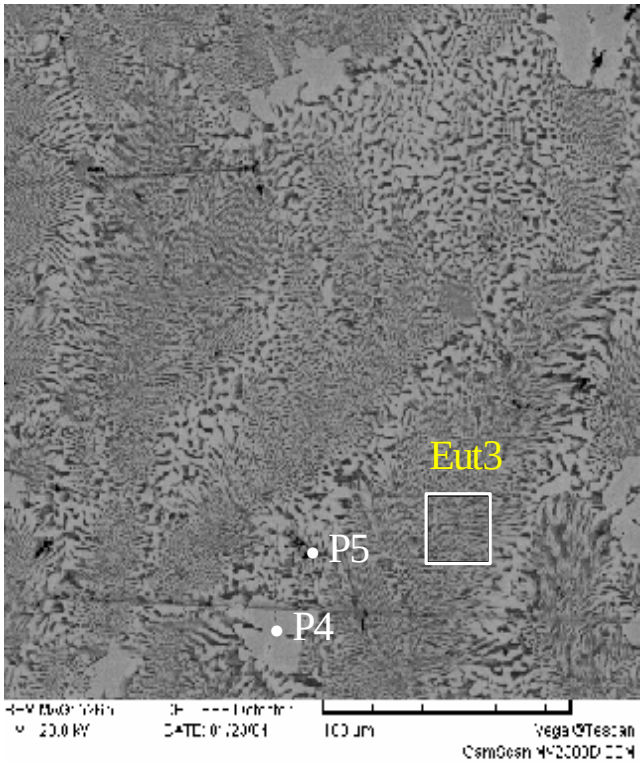

MC7 (SQ2)

Fig. 3.2. Microphotographs of MC6 and MC7 interaction zones

Table 3.1.

EDX analysis of the crystallized interaction zone

№		U	Zr	Fe	Cr	Ni	O
SQ1 (MC6)	mass.%	23.56	4.79	67.08	2.21	0.8	1.56
(1×1 mm)	mole%	6.57	3.49	79.74	2.82	0.91	6.47
Eut1 (MC6)	mass.%	38.53	1.04	56.5	1.24	1.21	1.48
(0.1×0.1 mm)	mole%	12.24	0.86	76.53	1.8	1.56	7
Eut2 (MC6)	mass.%	37.94	1.29	56.77	1.24	1.11	1.65
(20×20 μm)	mole%	11.93	1.06	76.09	1.79	1.42	7.72
SQ calc. (MC7)	mass.%	37.8	6.27	52.61	1.61	0.69	1.02
	mole%	12.45	5.38	73.82	2.43	0.92	5
SQ2 (MC7)	mass.%	44.33	2.17	50.06	1.59	0.73	1.12
(0.2×0.2 mm)	mole%	15.27	1.95	73.51	2.51	1.01	5.76
Eut3 (MC7)	mass.%	40.35	2.26	53.44	1.66	0.78	1.51
(20×20 μm)	mole%	13.13	1.92	74.12	2.47	1.04	7.33
P1 (MC6)	mass.%	-	-	95.94	3.7	-	0.36
	mole%	-	-	94.83	3.93	-	1.24
SQ3 (MC7)	mass.%	11.68	22.65	62.8	1.7	0.54	0.62
	mole%	3.26	16.52	74.84	2.17	0.61	2.6
P2 (MC6)	mass.%	22.57	22.09	51.79	0.64	1.06	1.85
	mole%	6.72	17.17	65.75	0.87	1.28	8.2
P3 (MC6)	mass.%	59.89	2.31	34.07	-	0.94	2.79
	mole%	23.36	2.35	56.62	-	1.49	16.18
P4 (MC7)	mass.%	55.62	4.85	37.21	-	0.84	1.47
	mole%	22.06	5.02	62.92	-	1.35	8.64
SQ4 (MC7)	mass.%	54.89	4.48	37.48	0.5	0.79	1.85
	mole%	21.16	4.51	61.6	0.88	1.24	10.61
P5 (MC7)	mass.%	2.01	93.24	1.31	-	-	3.44
	mole%	0.66	80.58	1.84	-	-	16.92
P6 (MC6)	mass.%	-	95.66	-	-	-	4.34
	mole%	-	79.45	-	-	-	20.55

The phases close (but not identical) in composition are: the tetrahedrally crystallized MC7 phase (Fig. 3.2, Table 3.1, SQ3) and MC6 interaction zone phase enriched with Zr (Fig. 3.2, P2).

Also close in composition: 1) phase, which forms a monolayer on the boundary with steel, and found in points between eutectics zones, (Fig. 3.2, SQ4 and P4) and 2) phase enriched with uranium (Fig. 3.2, P3, Table 3.1 P3). Phases P2 and P3 get crystallized like a continuous series of the UO_2 - ZrO_2 solid solutions (the boundary between phases is indistinct and one merges with another changing the composition).

The α-Zr-based phase is rare in the MC6 *interaction zone*, it concentrates near the boundaries of crystallized melt (in some locations of the "zone-crust" boundary the monolayer of this phase can be observed, e.g. Fig. 3.2, Table 3.1, point P6. It is even less frequent near steel; there it occurs as droplets and elongated crystals. In the MC7 *interaction zone* it is dispersed across the whole volume and concentrates in the interstices of eutectics, (Fig. 3.2, Table 3.1 point P5).

It can be assumed that the last two MC7 phases (Fig. 3.2, Table 3.1) are the phases, which constitute eutectics. It is not possible to separate the phases in the eutectics region by the EDX method for technical reasons: the structure is too fine.

Mechanism of steel-corium interaction

The interpretation of MC7 results is complicated, because the steady-state conditions have not been reached during the interaction. On the other hand, the available MC7 data are sufficient for making a number of important conclusions about the interaction dynamics, which would not be possible, if a steady state had been reached.

First, the interaction front profile observed in the test (Fig. 3.1) is an indicator of the spatial non-uniformity of the steel-corium interaction. Considerable difference of temperatures on the interaction boundary, additionally to the ultrasonic measurement data, confirms the unsteady state of the system at the time of test completion.

In view of this it can be asserted that the onset of the active interaction stage is restricted by the accumulation of a liquid phase on the crust – steel boundary, and the liquid phase is spread unevenly across the contact zone because of the irregular distribution of active components in the crust.

The crust is composed mostly of the phases based on α-Zr and on a continuous series of $U(Zr)O_2$ solid solutions. Probably one of the two mentioned phases provides a transport for the active component. In accordance with MC5 and MC6 data the active component is uranium, which has a low melting temperature and high diffusion mobility. In this way, the early stage of interaction is characterized by the diffusion of uranium (much less zirconium) into steel.

The α-Zr-based stage is likely to perform the function of a diffusion barrier for uranium, the zones of steel, which are less affected by the MC7 interaction, are located under the parts of crust, which are isolated by the α-Zr phase surrounding them.

The early interaction stage is followed by the accumulation of a liquid phase having eutectics composition, which corresponds to the incubation period observed in the test. Next stage in the process is a faster dissolution of steel at its contact with fusible multi-component eutectics.

This process slows down (in accordance with MC6 analysis) as the dissolution front approaches the isotherm surface in the specimen at a temperature corresponding to the temperature of the formed multi-component eutrectics.

Conclusions

1. The vessel steel ablation at its interaction with C-32 corium through the crust in argon atmosphere has been examined. During 10 hours the maximum temperature at the corium-steel interface was maintained at the 1150 °C level. The posttest examination of the steel specimen axial template has revealed: 1) distinct ***interaction zone*** and 2) ***thermal influence zone*** located under the interaction zone**.**

2. ***The interaction zone*** shaped as an irregular lens of solidified metallic melt is included into the body of the steel specimen to the depth of 3.1 mm from its top. It was produced by the mass-transfer processes between the liquid phases of corium components and steel, which were preceded by the diffusion saturation of steel by corium components with a primary formation of liquid metallic phase. The integral chemical composition of the solidified interaction zone melt has the following inventory and ratio of elements: U / Zr / Fe / Cr / Ni / Mn / Si / O = 43.95 / 2.15 / 49.63 / 1.58 / 0.72 / 0.45 / 0.4 / 1.11 (mass %). 80% of the crystallized melt structure have the following eutectic composition: U/ Zr/ Fe/ Cr/ Ni/ O = 40.35 /2.26 /53.44 /1.66 /0.78 /1.51 (mass %). The rest 20 % of the volume are composed by the grains from two metallic solid solutions, which can be described as $U(Zr)Fe_2(O)$ and $Fe_4(O)Zr(U)$.

   It has been established that all physico-chemical processes in the interaction zone occurred in the temperature interval of 1150 - 1095 ^oC, and the last value is close to the multicomponent eutectics (calculation error taken into account). At this the isotherm of the predicted final position of the interaction zone boundary is 1030-1100°C.

3. The steel destruction (ablation)/corrosion has been observed to go in three stages: a) Incubation period lasting 10000 seconds; b) Slow ablation period, which ended at the 18 000th second, during which steel ablated to form the eutectic liquid. The average speed of ablation at this stage was determined as $2{,}86 \times 10^{-5}$ mm/s. c) Intensive ablation period, which lasted to the end of the test, the 36000^{th} s., during which the steel was destructed by the volumetric eutectic liquid. The ablation rate at that stage was evaluated as 10^{-4} mm/s.

4. The numeric modeling of the specimen temperature field has been performed. The modeling enabled to evaluate the temperatures on the melt-specimen interaction front.

5. ***The zone of thermal influence*** occupies the 16-mm layer starting from the specimen top. It has the Widmanstatten pattern of the low-carbon steel in the zone of high-temperature influence next to the ***interaction zone***, and far from it, in the zone of incomplete annealing, it has the initial ferrite-pearlite structure with a slightly transformed grain size. The lower boundary of the thermal influence zone has a good coincidence with 760 ^oC isotherm, which was calculated during the specimen temperature field modeling. Such convergence proves the numeric model adequacy.

6. The MC7 results have been compared to the data of MC6, in which the temperature on the steel specimen top was maintained a little below 1400^o C. It has been confirmed that the steel ablation in both tests followed the same mechanism, which is steel dissolution in the superheated hypereutectic melt of Fe+U+Zr. In MC7 the interaction reactions were less intensive than in MC6. The following differences from MC6 have been found (MC6 data are in brackets):

- ***interaction zone*** *depth* is 3.1 mm (6.7 mm);

- ***thermal influence zone*** *depth* is 16 mm (24 mm);

- *ruptures* in the ***interaction zone*** are found in its whole volume (in MC6 the compact rupture is located off the specimen top center);

- *the integral composition* of ***the interaction zone*** is substantially enriched with U and Zr and has the $U(Zr)Fe_2(O)$ grain inclusions; (in MC6 the integral composition is enriched with Fe, and the structure contains dendrites of alloyed iron as the primary crystallization phases);

- the *incubation period* of the interaction process lasted 10 000 s, (2460 s.);

- *the stage of slow corrosion* was developing during a single period, which lasted ~ 8000 s., it had the rate of $3 \cdot 10^{-5}$ mm/s. (in MC6 this stage lasted 13500 s., it went in stages having different rates about 10^{-5} -10^{-4} mm/s.);

- *the fast corrosion(ablation) stage* started at the 18 000th s.; it had a relatively steady corrosion rate of 10^{-4} mm/s., and it had not been completed before the test was finished at the 36000th s.; (in MC6 this stage started at the 15960th s., the ablation rate was $8.75 \cdot 10^{-4}$ mm/s. at the linear stage having the duration of 4000 s., which gradually decreased to nil and finished at the 32000th s).

References

1. METCOR Work Plan, Phase 2.
2. Minutes of Meeting № 3 of the METCOR, Phase 2 Steering Committee.
3. Report on the modernization of the Rasplav-3 test facility (test Pr2-MC5), METCOR, Phase 2.
4. Yu. B. Petrov. Induction melting of oxides. L.: Energoatomizdat. Leningrad division, 1983. – 104 p.(In Russian)
5. Report on the vessel steel heat conductivity. METCOR, Phase 1.
6. A.P. Guliaev. Physical metallurgy. M.: Metallurghia, 1977.(In Russian)
7. Thermal treatment in machine building: Reference book / edited by Yu. M. Lakhtin, A.G. Rakhstadt – M. Mashinostroenie, 1980, 783 p. (In Russian)
8. METCOR-2 Annual report, №1-833.2-2003, 2004 г.
9. N.F. Losev. Quantitative X-ray fluorescence analysis. M. Nauka, 1969,366 p.
10. D.I. Riabchikov, M.M. Seniavin. Analytical chemistry of uranium. M. Publishing House of the USSR Academy of Sciences. 1962. (In Russian)
11. V.F. Lukianov, S.B. Savvin, I,V. Nikolskaya. Photometric detection of uranium microquantities using reagent arsenazo III. JACh., v. XV, issue 3. 1960. (In Russian)
12. RASPLAV Final Report. Attachment A. Post-test Examinations Methodology and Results Data published – July, 2000.
13. V.B. Khabensky et al. Methods of physico-chemical analysis // Intermediate report. NITI, MC-02/99, July 1999, (In Russian).
14. G.M. Butirin. High-porosity carbon materials.-M.: Chemistry, 1976,192 p. (In Russian).